

# 1    **Extensional reactivation of the Penninic Frontal Thrust 3 Ma ago as** 2    **evidenced by U-Pb dating on calcite in fault zone cataclasite.**

3  
4    Antonin Bilau<sup>a,b</sup>, Yann Rolland<sup>a,b</sup>, Stéphane Schwartz<sup>b</sup>, Nicolas Godeau<sup>c</sup>, Abel Guihou<sup>c</sup>, Pierre  
5    Deschamps<sup>c</sup>, Benjamin Brigaud<sup>d</sup>, Aurélie Noret<sup>d</sup>, Thierry Dumont<sup>b</sup>, **and** Cécile Gautheron<sup>d</sup>.

6    <sup>a</sup>EDYTEM, Université Savoie Mont Blanc, CNRS, UMR 5204, Le Bourget du Lac, France.

7    <sup>b</sup>ISTerre, Université Grenoble Alpes, Univ. Savoie Mont Blanc, CNRS, IRD, IFSTTAR, 38000  
8    Grenoble, France.

9    <sup>c</sup>Aix-Marseille Université, CNRS, IRD, INRAE, Collège de France, CEREGE, Aix en Provence,  
10    France.

11    <sup>d</sup>GEOPS, CNRS, Université Paris-Saclay, 91405 Orsay, France.

12    **Correspondence:** Antonin Bilau ([antonin.bilau@univ-smb.fr](mailto:antonin.bilau@univ-smb.fr)) and Yann Rolland  
13    ([Yann.Rolland@univ-smb.fr](mailto:Yann.Rolland@univ-smb.fr)).

## 14 15    **Abstract**

16    In the Western Alps, the Penninic Frontal Thrust (PFT) is the main crustal-scale tectonic structure of  
17    the belt. This thrust transported the high-pressure metamorphosed internal units over the un-  
18    metamorphosed European margin during the Oligocene (34-29 Ma). Following the propagation of the  
19    **compression** toward the European foreland, the PFT was later reactivated as an extensional  
20    detachment associated with the development of the High-Durance extensional fault system (HDFS).  
21    This inversion of tectonic displacement along a major tectonic structure has been widely emphasized  
22    as an example of extensional collapse of a thickened collisional orogen. However, the inception age of  
23    the extensional inversion remains unconstrained. Here, for the first time, we provide chronological  
24    constraints on the extensional motion of an exhumed zone of the PFT by applying U-Pb dating on  
25    secondary calcites from a fault zone cataclasite. The calcite cement/veins of the cataclasite, formed  
26    after the main fault slip event, at  $3.6\pm 0.4$ - $3.4\pm 0.6$  Ma. Cross-cutting calcite veins featuring the last  
27    fault activity are dated at  $2.6\pm 0.3$ - $2.3\pm 0.3$  Ma.  $\delta^{13}\text{C}$  and  $\delta^{18}\text{O}$  fluid signatures derived from these  
28    secondary calcites suggest fluid percolation from deep-seated reservoir at the scale of the Western  
29    Alps. Our data evidence that the PFT extensional reactivation initiated at least  $\sim 3.5$  Ma ago with a  
30    reactivation phase at  $\sim 2.5$  Ma. This reactivation may result from the westward propagation of the  
31    compressional deformation toward the External Alps, combined to the exhumation of External  
32    Crystalline Massifs. In this context, the exhumation of the dated normal faults is linked to the eastward  
33    translation of the HDFS seismogenic zone in agreement with the present day seismic activity.

## 34 **1. Introduction**

35 Dating of major tectonic inversions in orogens is generally achieved by indirect and relative dating,  
36 but rarely by the direct dating of fault-related minerals using absolute geochronometers. For instance,  
37 tectonic cycles are defined worldwide by the sediment unconformities or by exhumation ages through  
38 thermochronological investigation. However, the recent progress in U-Pb dating of carbonate using  
39 high-resolution Laser Ablation analyses (Roberts et al., 2020) allows us to directly date minerals  
40 formed during fault activity and thus to establish the age of tectonic phases by absolute radiometric  
41 dates (Ring and Gerdes, 2016; Goodfellow et al., 2017; Beaudoin et al., 2018;). This method is  
42 especially well suited to disentangle the successive tectonic motions along a given tectonic structure.  
43 U-Pb dating can be coupled to stable isotopic analysis to infer the nature of fluids through time, which  
44 may give insights of the scale of fluid circulations and thus the scale of the active tectonic structure  
45 and changes in the stress regime (e.g., Beaudoin et al., 2015; Rossi and Rolland, 2014). In the Western  
46 Alps, the Penninic Frontal Thrust or PFT represents a major thrust structure at lithospheric scale (e.g.,  
47 Tardy et al., 1990; Mugnier et al., 1993; Zhao et al., 2015) that accommodated the main collisional  
48 phase during the Paleogene-Neogene (e.g., Ceriani et al., 2001; 2004). Later on, this thrust was  
49 reactivated as a normal fault, and the extensional deformation is still ongoing (Sue and Tricart, 1999;  
50 Tricart et al., 2006; Sue et al., 2007). This transition from **compression** to extension in a collisional  
51 chain has been diversely interpreted to reflect slab breakoff, crustal overcompensation or post-glacial  
52 and erosion-induced isostatic rebound (e.g., Champagnac et al., 2007; Sternai et al., 2019). However,  
53 until now, no direct dating of the tectonic shift from **compression** to extension on the PFT has been  
54 obtained, which leads to many possible geodynamic scenari. At the present day, a large range of ages  
55 for this transition has been hypothesized from ~12 to 5 Ma (Tricart et al., 2006), to only few ten's ka  
56 (Larroque et al., 2009) which shows the lack of direct dating of brittle deformation (Bertrand and Sue,  
57 2017). In this study, we applied the Laser Ablation U-Pb dating method on secondary calcites from a  
58 cataclasite fault zone that testify of the extensional deformation of an exhumed paleo-normal fault  
59 during the PFT inversion.

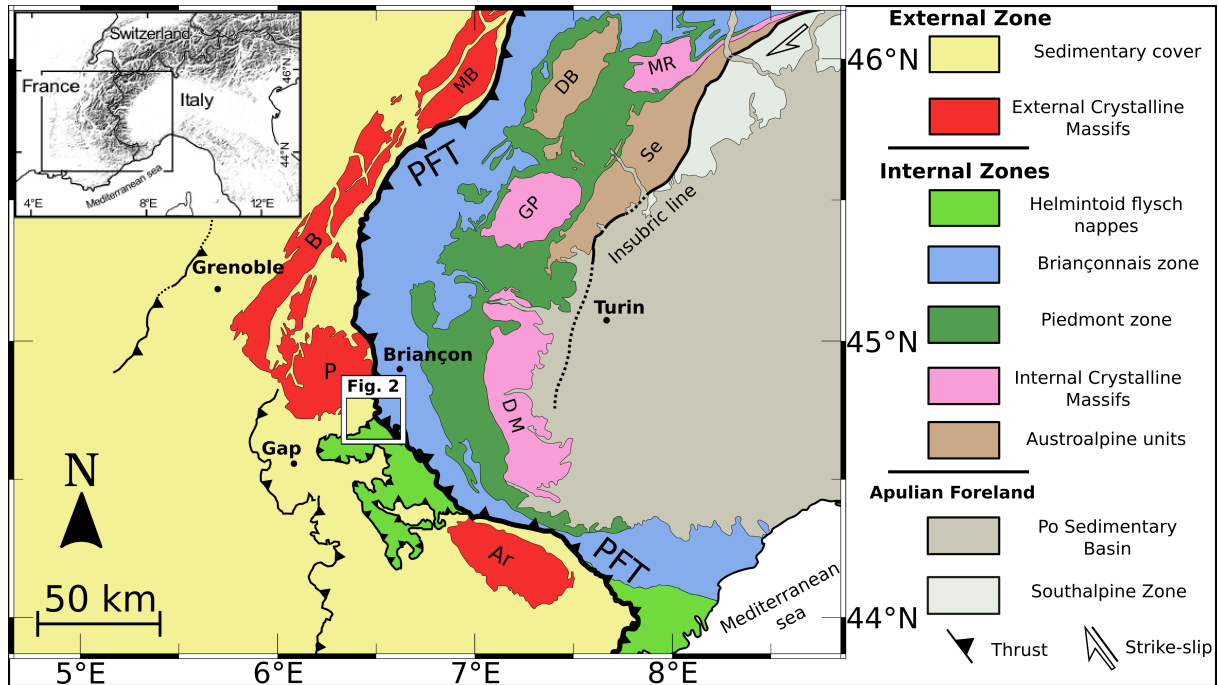
60 The purpose of this study is (1) to provide absolute chronological constraints on the structural  
61 inversion of the PFT, and (2) give insights into the scale and nature of fluid circulations along this  
62 major fault using stable isotope analysis of carbon and oxygen.

63

## 64 **2. Geological setting**

65 The western Alpine collisional belt results from the convergence and collision of the European and  
66 Apulian plates, which culminated with top-to-the west displacement on the PFT acting as the major  
67 Alpine tectonic structure in the Late Eocene to Oligocene times (e.g., Dumont et al., 2012; Bellahsen  
68 et al., 2014). This lithospheric-scale structure accommodated westward thrusting of highly

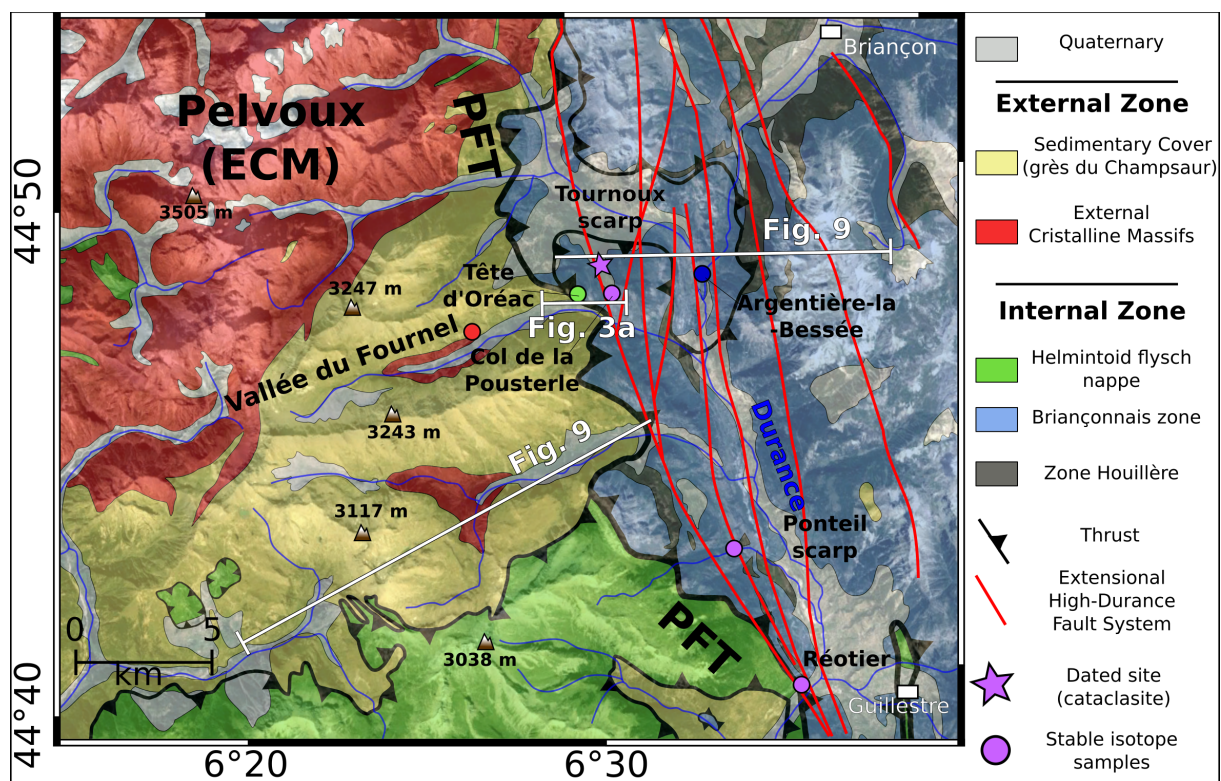
69 metamorphosed “Internal zone” units over slightly metamorphosed “External zone” units (Fig. 1,  
 70 Schmid and Kissling 2000; Lardeaux et al., 2006; Simon-Labric et al., 2009; Malusà et al., 2017). The  
 71 External zone is composed of the European non-metamorphosed Mesozoic and Paleozoic sedimentary  
 72 cover and its Paleozoic basement corresponding to the External Crystalline Massifs.



73  
 74 **Fig. 1.** Geological map of Western Alps showing the location of the study area. External Crystalline Massifs: Ar,  
 75 Argentera; B, Belledonne; MB, Mont Blanc; P, Pelvoux. Internal Crystalline Massifs: DM, Dora-Maira; GP,  
 76 Grand Paradis; MR, Mont Rose. PFT: Penninic Frontal Thrust. Insert modified from Schwartz et al. (2017).

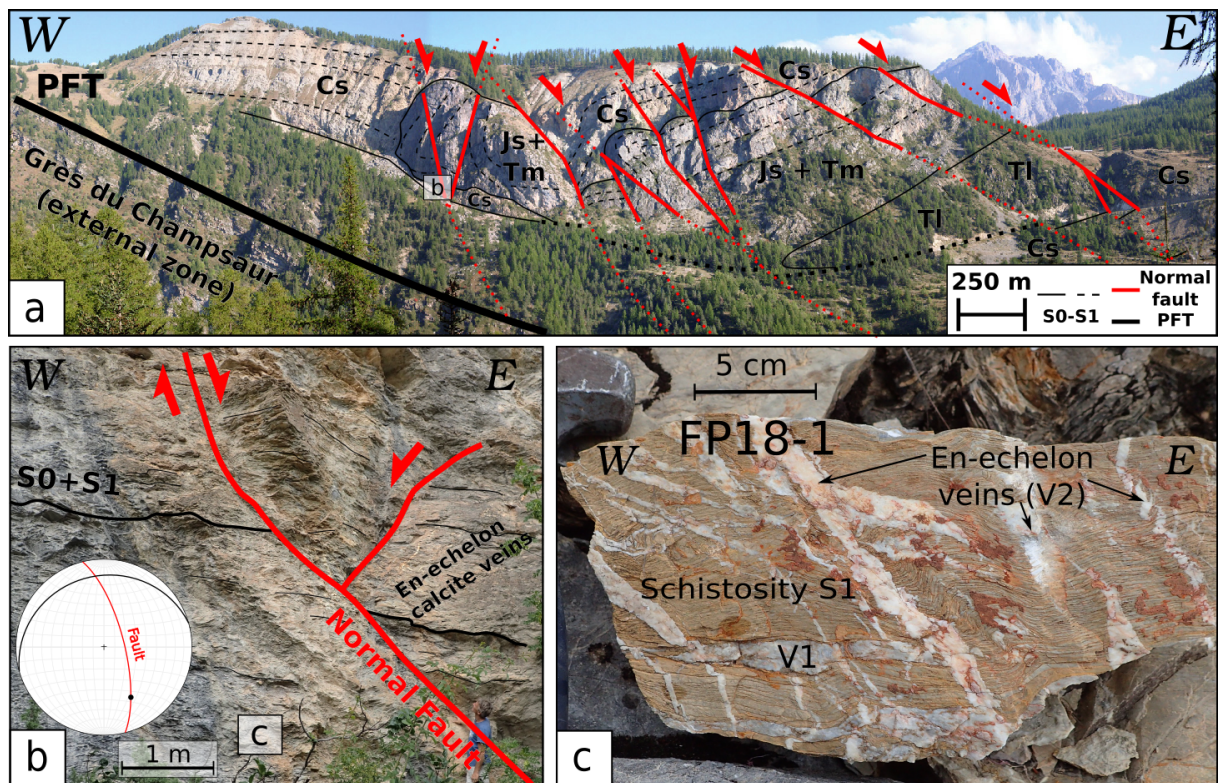
77  
 78 The Internal zone corresponds to a high-pressure metamorphic wedge formed by the stacking of the  
 79 paleo-distal European margin of the Briançonnais zone, comprising the Internal Crystalline Massifs  
 80 and their sedimentary cover, with the oceanic-derived units of the Piedmont zone. These units were  
 81 incorporated and juxtaposed in the subduction accretionary prism since the Early Late Cretaceous until  
 82 the Late Eocene (e.g., Agard et al., 2002; Schwartz et al., 2007). The timing of subduction and  
 83 collision is well constrained by numerous dates on metamorphic minerals (e.g., Duchêne et al., 1997;  
 84 Rubatto and Hermann, 2001; Lanari et al., 2012, 2014). Eclogite facies recrystallization records  
 85 subduction of the distal European margin at  $32.8 \pm 1.2$  Ma in the Dora Maira massif, which was later  
 86 transported as a tectonic nappe during the collision (Duchêne et al., 1997). PFT activation and  
 87 underthrusting of External Crystalline Massifs are indicators of the transition from subduction to  
 88 continental collision in the Internal zones, between 44 and 36 Ma (e.g., Beltrando et al., 2009). This  
 89 transition is marked by shear zone development at greenschist facies conditions and recrystallization  
 90 during burial of the Alpine External zone in the PFT footwall compartment (Rossi et al., 2005;  
 91 Sanchez et al., 2011; Bellahsen et al., 2014). The early ductile PFT activity is dated at 34-29 Ma by

92  $^{40}\text{Ar}/^{39}\text{Ar}$  dating of syn-kinematic phengite from shear zones in the Pelvoux and Mont Blanc External  
 93 Crystalline Massifs (Seward and Mancktelow, 1994; Rolland et al., 2008; Simon-Labric et al., 2009;  
 94 Bellanger et al., 2014; Bertrand and Sue, 2017) and by U-Pb on allanite (Cenki-Tok et al., 2014). The  
 95 age of the PFT hanging wall tectonic motion and joint erosion is highlighted by the exhumation of the  
 96 Briançonnais units constrained by apatite fission tracks (AFT) at 26-24 Ma (Tricart et al., 1984, 2001,  
 97 2007; Ceriani and Schmid, 2004). However, the PFT reactivation as a normal fault remains  
 98 unconstrained. The onset of PFT extensional activity has been proposed to the Late Miocene (~12 to 5  
 99 Ma), based on indirect AFT ages in the Pelvoux External Crystalline Massif (Tricart et al., 2001,  
 100 2007), that record a cooling episode related to relief creation and erosion. The current seismicity (e.g.,  
 101 Rothé, 1941; Sue et al., 1999, 2007) and observed GPS motions (Walpersdorf et al., 2018; Mathey et  
 102 al., 2020), all along the so-called High-Durance Fault System (HDFS) highlight the fact that  
 103 extensional and minor strike-slip deformations along the PFT are still ongoing. This seismicity mostly  
 104 occurs at shallow depths, less than 10 km, and mainly at 3 to 8 km, where the HDFS is structurally  
 105 connected to the PFT (Sue and Tricart 2003, Thouvenot and Fréchet, 2006; Sue et al., 2007).



106 **Fig. 2.** Study area of the Penninic Frontal Thrust, east of the Pelvoux External Crystalline Massif (ECM). High-  
 107 Durance Fault System is represented in red from Tricart et al. (2001) and Sue et al. (2007). Location of sampled  
 108 sites is indicated. The location of the extensional fault dated by U-Pb on calcite (samples FP18-2 and FP18-3) is  
 109 marked by a star. Colour of site circle refers to the host rock age: red, Eocene sandstone flysch (grès du  
 110 Champsaur); green, Cretaceous carbonates; blue, Jurassic carbonates; purple, Triassic carbonates. Sample  
 111 descriptions are shown on Suppl. Mat. 1. © Google Earth for background relief map.

112 The study area is focused on a portion of the PFT located in the southeast of the Pelvoux External  
 113 Crystalline Massif in the Western Alps (France) (Figs. 1-2). Here, the PFT rests on Late Eocene  
 114 (Priabonian) autochthonous nummulitic flysch so-called the “Champsaur sandstone” (Fig. 2), which lies  
 115 unconformably on the Pelvoux crystalline basement. In the southern part, the PFT lies on the  
 116 Cretaceous Helminthoid flysch nappes, Fig. 2. These two flysch units are intensely deformed by top-to-  
 117 the-west PFT **compressional** deformation. The PFT hanging wall corresponds to the Briançonnais zone  
 118 composed of Mesozoic and Paleozoic sedimentary units, which underwent high pressure  
 119 metamorphism (Lanari et al., 2012; 2014). The Briançonnais zone is composed of the Briançonnais  
 120 Zone Houillère, which consists of Carboniferous sediments overlying a crystalline basement,  
 121 stratigraphically overlain by Middle Triassic to Cretaceous sediments (limestones and calcschists). The  
 122 PFT structure is well shown in the Tête d’Oréac section of the Fournel Valley transect (Fig. 3, Sue and  
 123 Tricart, 1999). Here, normal faults cross-cut the Briançonnais series and branch down on the PFT,  
 124 which was reactivated as a detachment (Tricart et al., 2001).



125 **Fig. 3. a:** General view and geological interpretation of the Fournel Valley southern slope with the studied site  
 126 of the Tête d’Oréac. **b:** Outcrop interpretation of the Tête d’Oréac with extensional features in late Cretaceous  
 127 calcschists in agreement with the High-Durance Fault System and Wulff stereogram, lower hemisphere. **c:**  
 128 Calcschist oriented sample FP18-1 evidencing multiple calcite vein generations. V1 is related to the main  
 129 **compressional** phase related to the Tête d’Oréac anticline formation and V2 are related to extensional  
 130 reactivation of the PFT during onset of the High-Durance Fault System. Cs: Late Cretaceous calcschists;  
 131 Js+Tm: Middle Triassic to Late Jurassic dolomitic to siliceous limestones; Tl: Lower Triassic sandstones.

132 The normal faults are tilted by a passive rotation of about 30 degrees towards the west during their  
133 exhumation in relation with the activity of the High-Durance Fault System (Sue et al., 2007).

134

### 135 **3. Sampling strategy and analytical methods**

#### 136 *3.1. Sampling strategy*

137 We collected key samples of each brittle-ductile deformation phase, both in the PFT footwall and  
138 hanging wall (Suppl. Mat. 1), to provide a petrographic and stable isotopic dataset which will allow  
139 discussing the nature of fluids throughout the PFT activity associated to the late **compressional** and  
140 extensional history. Field analysis is supported by petrographic observations on 28 samples, including  
141 8 host rocks, 6 from compressive structures and 14 from extensive structures. Based on this dataset,  
142 we selected three fault breccia samples to date the PFT extensional reactivation.

143

#### 144 *3.2. Cathodoluminescence*

145 Cathodoluminescence (CL) analysis provides shades that are mainly representative of oxidation state  
146 of trace element and their contents, i.e. Mn<sup>2+</sup> and Fe<sup>2+</sup> (Barnaby and Rimstidt, 1989). These differences  
147 in calcite chemical composition are an indicator of different mineral precipitations related to slight  
148 variations in fluid composition (Goodfellow et al., 2017). CL can also highlight crystal growth patterns  
149 or grain boundary interactions (Beaudoin et al., 2015). Using cross-cutting criteria as well as CL, a  
150 relative chronology of the calcite generations and related microstructures has been made. Analyses  
151 were performed with a spot camera mounted-Cathodyne device (cold cathode) with the following  
152 parameters: vacuum ~50mTorr; voltage 16-18 kv; electron beam ~200 μA. Used description  
153 terminology is based on Bons et al. (2012).

154

#### 155 *3.3. O and C stable isotope analysis*

156 Stable isotope measurements were achieved on the different generations of microstructures identified  
157 by thin section observations and CL images, at Geosciences Paris Sud (GEOPS) laboratory of the  
158 Paris-Saclay University, France. Results are presented in Table 1. The protocol is described in detail by  
159 Andrieu et al. (2015). Several milligrams (~1mm<sup>3</sup>) of sample for each calcite generation were  
160 collected using a Dremel 4000 with a 3.2 mm head. Samples were then dissolved with pure  
161 orthophosphoric acid (H<sub>3</sub>PO<sub>4</sub>): Sample tubes provided with two compartments (one for the sample and  
162 one for the acid) were sealed under a pressure of 1.5x10<sup>-2</sup> mbar. They were immersed in a water bath at  
163 25°C before the acid was poured on the sample and let to react for 24 h. Complete reaction is  
164 necessary to avoid any artificial isotopic fractionation. The produced CO<sub>2</sub> is collected using an  
165 extraction line and a liquid nitrogen trap is used to ensure that only CO<sub>2</sub> is collected. Pure CO<sub>2</sub> is  
166 analyzed on a VG Sira 10 dual inlet IRMS (Isotope Ratio Mass Spectrometer). Data validity is

167 supported by concurrent analysis of the international standard IAEA CO-1.  $\delta^{13}\text{C}$  and  $\delta^{18}\text{O}$  are  
168 expressed in ‰ relative to V-PDB (Vienna Pee Dee Belemnite) by assigning a  $\delta^{13}\text{C}$  value of +1.95‰  
169 and a  $\delta^{18}\text{O}$  value of -2.20‰ to NBS19, (1).

$$170 \quad \delta^{13}\text{C} = \left[ \frac{(^{13}\text{C}/^{12}\text{C})_{\text{Sample}}}{(^{13}\text{C}/^{12}\text{C})_{\text{Reference}}} - 1 \right] \times 1000 \quad (1).$$

171 For oxygen isotope measurements, switch from PDB values to SMOW (Standard Mean Oceanic  
172 Water) were made using the Kim et al. (2015) equation, (2).

$$173 \quad \delta^{18}\text{O}_{\text{SMOW}} = 1.03086 \times \delta^{18}\text{O}_{\text{PDB}} + 30.86 \quad (2).$$

174 The ratio of carbon and oxygen isotopes is related to the parental fluid of calcite and can be used as a  
175 fluid tracer. Reproducibility was checked by replicate analysis of in-house standards and was  $\pm 0.2\%$   
176 for oxygen isotopes and  $\pm 0.1\%$  for carbon isotopes.

177

### 178 *3.4. U-Pb dating of calcite*

179 In-situ uranium and lead isotope analyses of carbonates were carried out at CEREGE (Centre  
180 Européen de Recherche et d'Enseignement des Géosciences de l'Environnement), Aix-en-Provence,  
181 France. Results are presented in Suppl. Mat. 2. Data were acquired on 150  $\mu\text{m}$  thick thin sections.  
182 Laser ablation analysis was performed with an ESI excimer Laser Ablation system with a 6 inches two  
183 volume cell (ESI), coupled to an Element XR SF-ICP-MS (Sector Field Inductively Coupled Mass  
184 Spectrometer, Thermo-Scientific). Analyses were done at 10 Hz and 1.1-1.15  $\text{J}\cdot\text{cm}^{-2}$ . Samples were  
185 first screened to check signal intensities and maximise the spread of  $^{238}\text{U}/^{206}\text{Pb}$  ratios (e.g. map of  
186 Suppl. Mat. 3) to obtain the highest U-Pb variability. A typical analysis consists of 3 seconds of pre-  
187 ablation to clean the sample surface, followed by 20 seconds of gas blank and  $\sim 20$  seconds of  
188 measurement on a static circle spot of 150  $\mu\text{m}$  diameter (approximately 8-9 acquisition cycles per  
189 second). These parameters lead to approximately  $\sim 20\text{-}25$   $\mu\text{m}$  depth hole ( $\sim 1$   $\mu\text{m}/\text{s}$ ) on a carbonate  
190 material. Ablated particles are carried out of the cell with a He gas flux of 1300 ml/min and then  
191 mixed with Ar sample gas (typically 0.8-0.9 l/min). Unknown samples were corrected by standard  
192 bracketing with synthetic NIST-614 glass for instrumental drift and lead isotope composition  
193 (Woodhead et al. 2001) and a natural calcite spar WC-1 of  $254.4 \pm 6.4$  Ma (Roberts et al., 2020) for  
194 inter-elemental fractionation effect, every 20 measurements. No downhole correction was applied  
195 since no natural calcite standard with homogeneous U-Pb ratio allows such correction. However, the  
196 large aspect ratio used in this set up is supposed to limit this effect. Unknown sample were first  
197 processed with the Iolite software (Paton et al., 2011) for baseline correction. Raw ratios were then  
198 reduced for instrumental drift, lead isotope composition and inter-elemental fractionation using an in-  
199 house excel spreadsheet macro designed for carbonate samples. Ages are obtained using IsoplotR  
200 software and plotted in a Tera-Wasserburg diagram using model (1) age (Vermeesch, 2018). An

201 additional error propagation of 2.51% in quadratic addition on the final age, tied to the WC-1 standard,  
 202 is expressed in brackets in the Tera-Wasserburg plot.

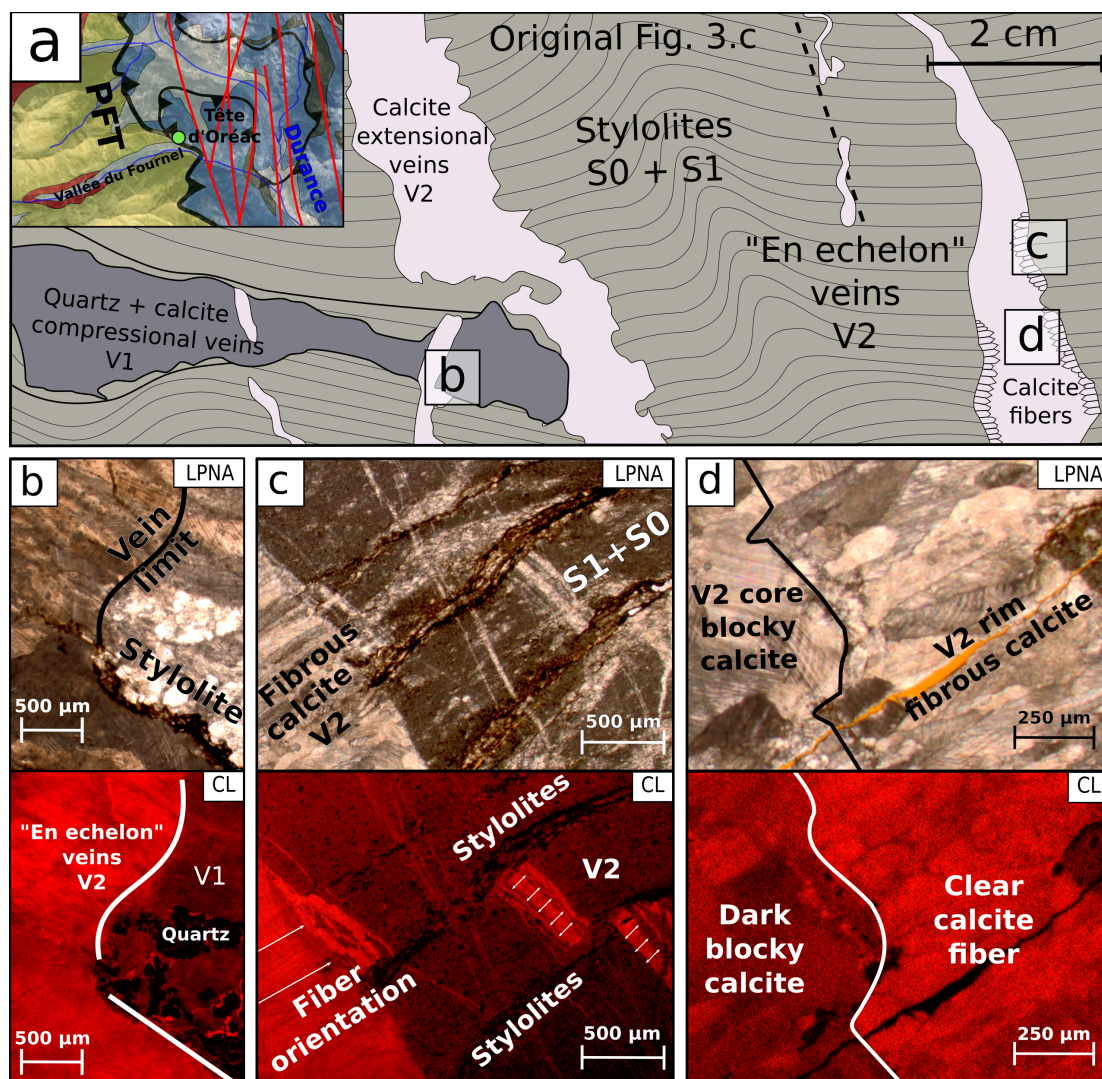
203

## 204 4. Results

### 205 4.1. Deformation phases and microstructures

#### 206 4.1.1. Brittle-ductile deformation features

207 During the westward thrust motion, the Tête d'Oréac cross-section passes through the PFT (Fig. 3) and  
 208 preserves a succession of units that were stacked on each other during to the west thrust motion of the  
 209 PFT. The main schistosity (S1) is parallel to the initial bedding (S0) in Cretaceous calcschists. S0-S1 is  
 210 sub-horizontal and penetrative throughout the studied area. At the outcrop scale, S1 is clearly visible  
 211 and shows dissolution surface with the development of stylolitic joints (Fig. 4).



212 **Fig. 4. a:** General sketch of sample FP18-1 evidencing cross-cutting relationships for two main vein generations  
 213 **fig. 3.c. b-d:** Microscope and cathodoluminescence pictures showing the different vein calcite generations.

214 Quartz anisotropy is observable in LPA which indicate an important deformation syn-post V1. This  
215 correlate a strong transposition of structures during PFT compressive motion or opened initially near  
216 parallel to S1 either way a ductile deformation is recorded. These early **compressional** features are  
217 cross-cut by numerous steeply dipping eastward normal faults linked to the extensional reactivation of  
218 PFT. Early stages of extension are featured by centimetre scale “en-echelon” veins (V2) indicative of  
219 an early brittle-ductile extensional deformation followed by dissolution on the horizontal composite  
220 (S0-S1) cleavage. Larger V2 veins, expressed at centimetre scale, cross-cut the cleavage and show  
221 elongated calcite fibres of ~1000 µm at the vein walls (Fig. 4). Similar shades for early V2 and fibrous  
222 V2 are observed in CL. At vein cores, the fibrous calcite is then replaced by a blocky calcite that is  
223 less luminescent in CL.

224

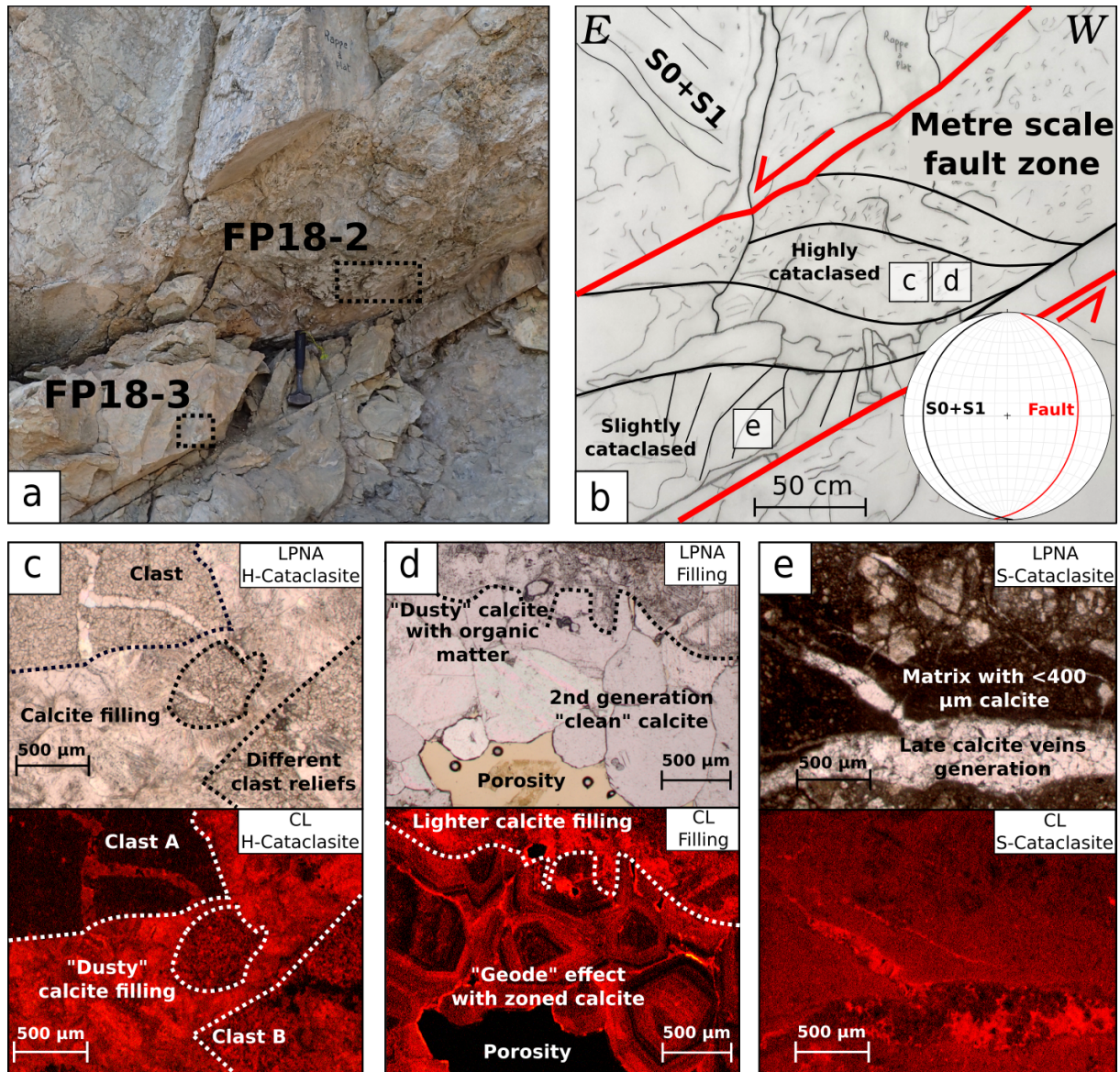
#### 225 4.1.2. Brittle deformation features

226 The internal structure of one major extensional fault is investigated in the Tournoux scarp (Fig. 5). The  
227 fault zone is highlighted by a metre-scale cataclasite fault gouge with variable amounts of  
228 deformations. The top-to-the East (N90°E) normal sense of shear is represented by sigmoids and  
229 down-dip slickenside. At thin-section scale, for sample FP18-2, the cataclasite is composed of  
230 centimetre-scale host rock clasts with very small (<20 µm) limestone grains. Two types of calcite  
231 fillings have been identified. The first one contains organic matter has a « dusty appearance » with  
232 bright shades in CL (Fig. 5C). The second one shows large and clear crystals that grew in the cracks  
233 and porosity, showing sector zoning patterns highlighted in CL and Laser Ablation-Inductively  
234 Coupled Plasma-Mass Spectrometry (LA-ICP-MS) maps (Fig. 5D; Suppl. Mat. 3). ~700 µm large  
235 hexagonal, clear and organic matter free, calcite crystals have been selected for U-Pb dating.

236 These calcite crystals represent the latest pervasive fluid circulation episode through the porosity and  
237 provide a minimum age for the cataclasite. In sample FP18-3, the matrix is cross-cut by calcite veins  
238 with variable diameters (300-1300 µm) and is free of any further deformation. On the basis of their  
239 homogeneity and their youngest relative age relationships, these late calcites have also been targeted  
240 for U-Pb calcite dating (see section 4.3). Samples FP19-12A-B (described in supplementary data)  
241 were collected in a west-dipping conjugate normal fault and exhibits similar deformation features.

242

243 **Fig. 5. a-b:** Outcrop interpretation of the Tournoux scarp showing various degrees of cataclasis in Triassic  
244 dolomitic limestone with Wulff stereogram lower hemisphere. Squares are sampled area, sample FP18-2 is a  
245 highly cataclased sample, while sample FP18-3 is less intensely cataclased and is cross-cut by millimeter-scale  
246 calcite veins. **c, d, e:** Microscope and cathodoluminescence pictures showing several calcite filling generations.  
247 « clear calcite » shows zonings and seems to crystallize into a primary porosity left within the cataclasite. The  
248 clear calcite and veins from the cataclasite are dated using the U-Pb dating on calcite method.

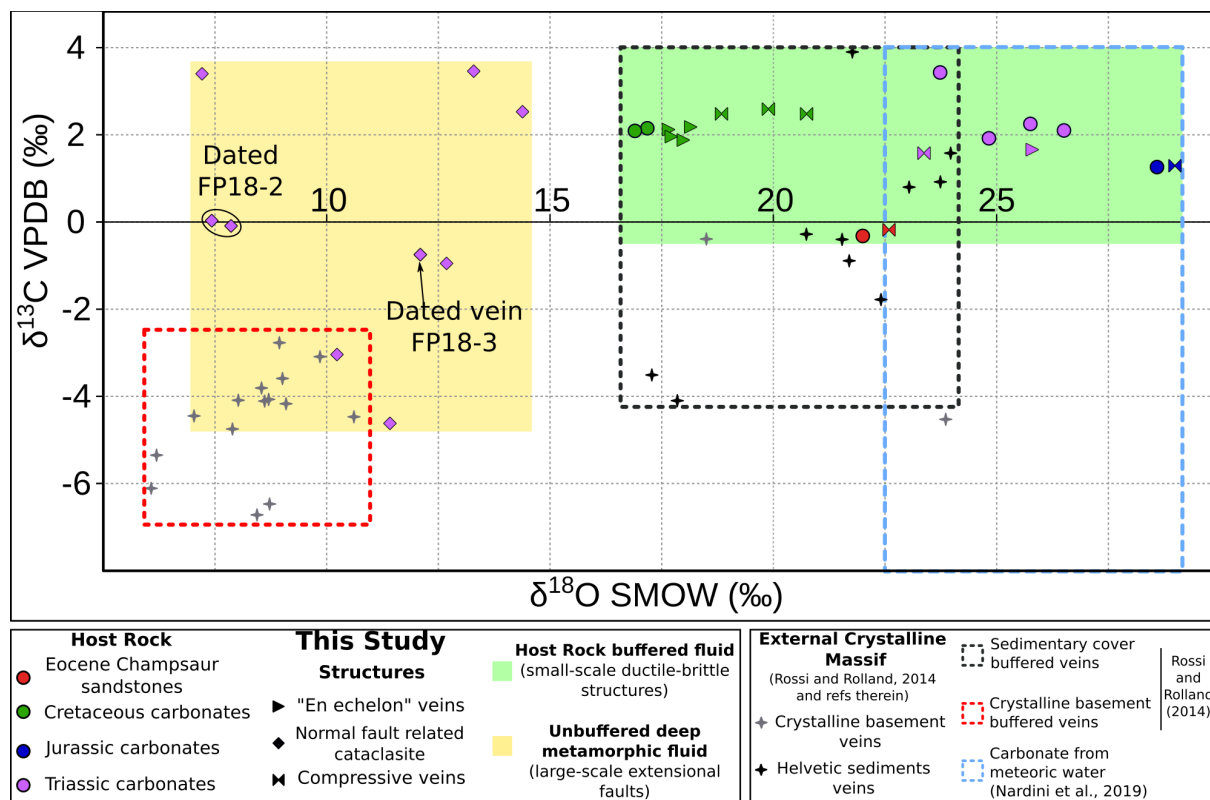


250 4.2.  $\delta^{13}\text{C}$  and  $\delta^{18}\text{O}$  stable isotope results

251 Stable isotopes analyses were performed in calcites from various host rocks samples belonging to the  
 252 different units highlighted in the studied PFT section (Fig. 3) and are supposed to be representative of  
 253 the different (compressional and extensional) key tectonic phases (Fig. 6).

254 For host rock analysis, upper Cretaceous planktonic calcschists from the Tête d'Oréac show the lowest  
 255  $\delta^{18}\text{O}$  host rock value of 16.8-17.1 ‰ and of  $\delta^{13}\text{C}$  of 2.1-2.2 ‰. Triassic carbonates show a range  
 256 between 23.7-26.5 ‰ for  $\delta^{18}\text{O}$  and between 1.9-2.3 ‰ for  $\delta^{13}\text{C}$  (with a higher value of 3.4 ‰ for the  
 257 Ponteil scarp). Upper Jurassic calcschists gave  $\delta^{18}\text{O}$  ratio of 28.5 ‰ and  $\delta^{13}\text{C}$  of 1.3 ‰. The western  
 258 Late Eocene Flysch (Champsaur sandstone) gave lowest  $\delta^{13}\text{C}$  ratio of -0.3 ‰ and a  $\delta^{18}\text{O}$  ratio of 21.9  
 259 ‰. Analysed brittle-ductile veins either related to the compressional or to the onset of the extensional  
 260 tectonic phases stand very close to their host rocks, near to the meteoric water field defined by Nardini

261 et al. (2019) (Fig. 6). However, the V2 veins associated to the brittle normal fault development, clearly  
 262 show lower  $\delta^{18}\text{O}$  values (<15‰) compared to their host rocks, with a trend towards lower  $\delta^{13}\text{C}$  values.  
 263 These isotope signatures are similar to those measured in calcite from veins of the Mont Blanc  
 264 External Crystalline Massifs (Rossi and Rolland, 2014).

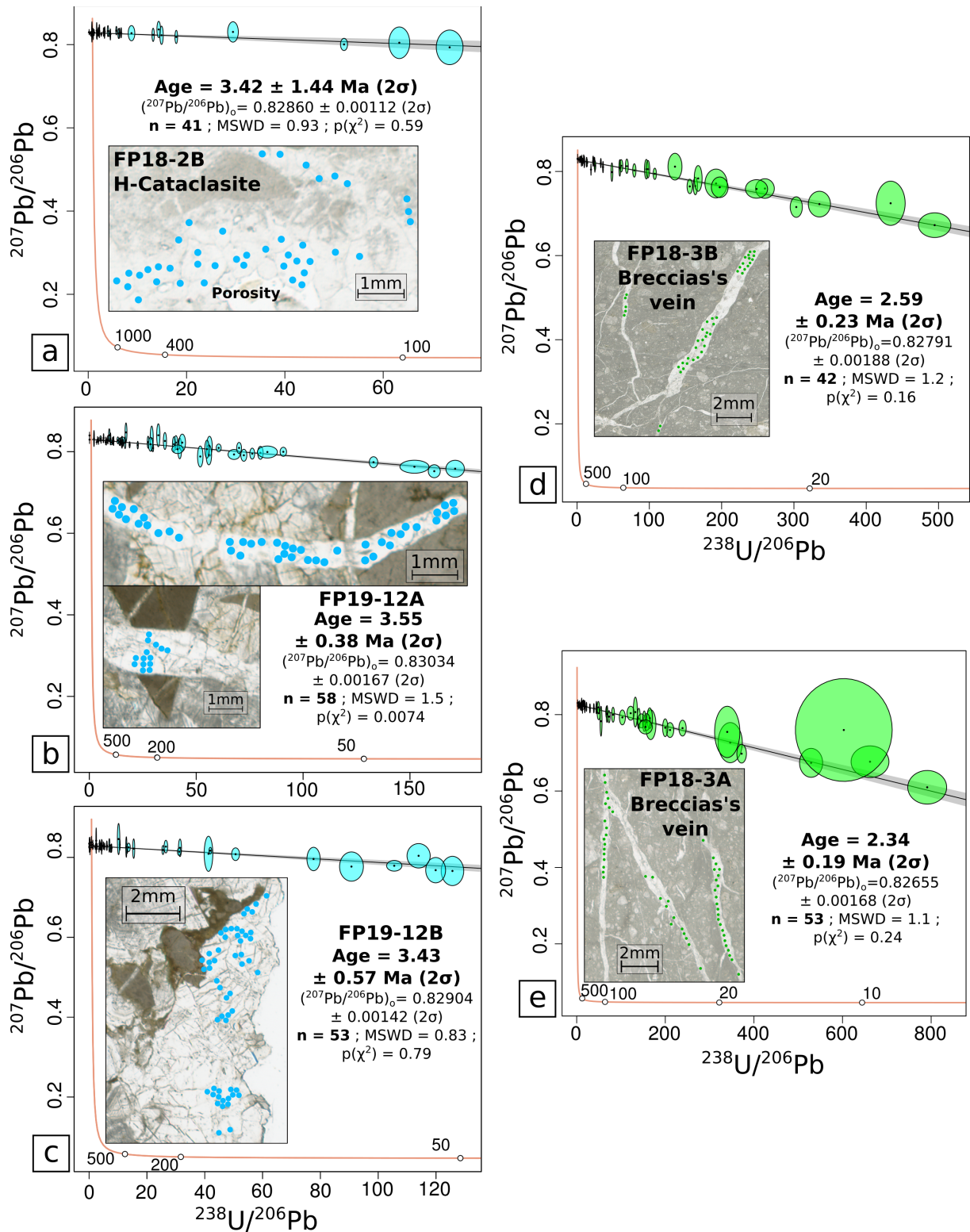


265 **Fig. 6.** Stable isotopic data from samples indicated on Fig. 2. Domains represented by dashed red, black and  
 266 blue lines are from the literature (Nardini et al., 2019; Rossi and Rolland, 2014 and references therein). The  
 267 coloured green domain corresponds to veins associated to brittle-ductile structures. These veins show similar  
 268 isotopic compositions as their host rocks. The orange domain features the signature of cataclased normal fault  
 269 samples, which show a different isotopic composition as compared to their host rock, and are similar to deep  
 270 metamorphic fluids (e.g., Crespo-Blanc et al., 1995; Rossi and Rolland, 2014; Rolland and Rossi, 2016).

271

#### 272 4.3. Calcite LA-ICPMS U-Pb dating results

273 Petrographic analysis has been complemented by screening using LA-ICP-MS on 24 thin-sections  
 274 from samples of 7 locations around the PFT related to compressive and extensive structures. Among  
 275 these, 20 screened samples show high common lead contents, and sometimes higher lead to uranium  
 276 intensity signals. U-Pb dating of such carbonates with high lead concentrations remains highly  
 277 challenging, especially for very young samples. However, four samples (samples FP18-2, 3 and FP19-  
 278 12A&B described in section 4.1 and supplementary data) from the Tournoux normal fault site bear  
 279 sufficient  $^{238}\text{U}$  (~0-8.5 ppm for FP18-3A&B and ~0-4.5 ppm for FP18-2B and FP19-12A&B), and  
 280  $^{206}\text{Pb}$ ,  $^{207}\text{Pb}$  (~0-1.9 ppm for FP18-3A&B and ~0-13.1 ppm for FP18-2B and FP19-12A&B).



281 **Fig. 7.** Tera-Wasserburg concordia plot of (a) Highly cataclased sample FP18-2 calcite filling (b) and (c)  
 282 sample FP19-12A veins and FP19-12A 'clean calcite' filling (d) and (e) sample FP18-3 veins, and  
 283 corresponding maps of sampled spots (150  $\mu\text{m}$ ). MSWD: Mean Square Weighted Deviation. An additional error  
 284 propagation tied to WC-1 standard uncertainty is taken into account.

285

286 Lead contents are based on NIST614 intensities and uranium contents are based on WC-1 intensities  
287 (Jochum et al., 2011; Roberts et al., 2017; Woodhead et al., 2001), giving measurable and significant  
288 radiogenic signal. Five ages have been obtained on these four samples (Fig. 7).

289 A first group of ages of ~3.5 Ma is represented by three samples. The cataclasite ‘clean calcite’ infill  
290 (sample FP18-2B; Fig. 5) gives age of  $3.42 \pm 1.44$  Ma ( $n=41$ ,  $MSWD=0.93$ ). This quite large  
291 uncertainty is due to a relatively moderate U/Pb variability and the resulting low radiogenic signal  
292 measurable in this sample. Samples FP19-12A&B give two similar within-error ages for the vein  
293 calcite and ‘clean calcite’ infill, of  $3.55 \pm 0.38$  ( $n=58$ ,  $MSWD=1.5$ ) and  $3.43 \pm 0.57$  ( $n=53$ ,  
294  $MSWD=0.83$ ), respectively.

295 A second group of ages of ~2.5 Ma is obtained on different cross-cutting veins of the latest generation  
296 of sample FP-18-3 (Fig. 5), represented by slightly younger, but distinct out of error margins, ages of  
297  $2.59 \pm 0.23$  Ma ( $n=42$ ,  $MSWD=1.2$ ; FP-18-3B in Fig. 7b) and  $2.34 \pm 0.19$  Ma ( $n=53$ ,  $MSWD=1.1$ ; FP-  
298 18-3B in Fig. 7c). The higher spread in U/Pb ratios measured in these two latter ages results in more  
299 precise and robust ages. These two age groups obtained on extensional faults connected to the PFT  
300 highlight for the first time at least two phases of deformation constrained out of error bars: a first  
301 phase of brittle deformation forming the cataclasite at  $3.5 \pm 0.4$  and one or two discrete brittle events at,  
302 or comprised within,  $2.6 \pm 0.2$  and  $2.3 \pm 0.2$  Ma. These ages show that the sated conjugated faults have  
303 been active for at least 1 Myr, and are featured by only several datable events, representing co-seismic  
304 motions on the faults.

305

## 306 5. Discussion

307 Onset of extensional tectonics in the Alps has remained a topic of debate for the last 20 years. A  
308 Miocene age has been proposed for the onset of the extensional activation of the PFT based on AFT  
309 datings on both sides of this major fault, i.e. in the Pelvoux External Crystalline Massif and in the  
310 Champsaur sandstones to the west and in the Briançonnais zone to the east (Tricart et al., 2001; 2007;  
311 Beucher et al., 2012). The Briançonnais zone corresponds to the east hanging wall compartment of the  
312 PFT. In this compartment, AFT ages ranging from 30 Ma to 20 Ma are interpreted as the exhumation  
313 age of this area related to the **compressional** activity of the PFT during the Alpine collision, which  
314 motion is constrained by direct  $^{40}\text{Ar}/^{39}\text{Ar}$  dating on phengite at 35-25 Ma (Simon-Labric et al., 2009;  
315 Bellanger et al., 2015). To the west (footwall of the PFT), the AFT ages range from 13 Ma to 4 Ma in  
316 the Pelvoux External Crystalline Massif (Beucher et al., 2012), and from 9 to 4 Ma in the Champsaur  
317 sandstones (Tricart et al., 2007), and are interpreted as the extensional reactivation of the PFT by these  
318 latter authors. As the AFT dates record an exhumation age associated with cooling below ~100°C  
319 (Ault et al., 2019), they may not correspond to an age of PFT activity but rather record an erosion  
320 process that is related to both climatic and tectonic processes (e.g., Champagnac et al., 2007). Sternai

321 et al. (2019) suggest that vertical movement in the Western Alps may be mainly ascribed to erosion  
322 and deglaciation (Nocquet et al., 2016) and may also include a significant mantle convection  
323 component (Salimbeni et al., 2018). However, the External Crystalline Massifs exhumation was also  
324 driven by frontal thrusting, activated during middle Miocene at the western front of these massifs  
325 (Boutoux et al., 2015) and by strong erosional processes that enhanced exhumation since the Late  
326 Miocene (Cederbom et al., 2004). Along the PFT, younger AFT and phengite  $^{40}\text{Ar}/^{39}\text{Ar}$  ages of ~10 Ma  
327 were obtained on the Plan de Phasy (Guillestre) metagranite mylonites (Tricart et al., 2007; Lanari et  
328 al., 2014). These ages have been interpreted as the result of hydrothermal fluid circulation, which may  
329 be linked to tectonic activity of the High-Durance Fault System. However these fluid circulations may  
330 be passive through the PFT network and may not correspond to extension onset. Therefore, the age of  
331 PFT activity remains unconstrained and requires some direct datings. In the following discussion, we  
332 show how absolute U-Pb dating of fracture infill calcite brings quantitative time constraints on PFT  
333 fault movement.

334

#### 335 *5.1. Deformation and scale of fluid flow in the brittle-ductile structures*

336 The measured  $\delta^{18}\text{O}$  and  $\delta^{13}\text{C}$  isotope ratios of veins from brittle-ductile structures are close or similar  
337 to their host rocks, and remain close to the field of carbonates precipitated from meteoric water  
338 (section 4.2). Based on several studies in the frontal parts of Alpine orogens (Smeraglia et al., 2020;  
339 Nardini et al., 2019), these isotope signatures are thought to be representative of meteoric water inflow  
340 from the most superficial domains. Three important parameters are involved to control this surface-  
341 derived fluid regime: (i) lack of large-scale structures (ii) pressure-solution microstructures (evidence  
342 of local fluid) (iii) presence of a shallow impermeable clay-rich layers which isolate upper crust from  
343 more deeply-rooted systems (section 4.1. and Fig. 3). Rossi and Rolland (2014) report similar stable  
344 isotope signatures in the Mont Blanc External Crystalline Massif sedimentary cover (Helvetic schists).  
345 There, the vein calcites bear similar stable isotope values as the host Helvetic schists, which is in  
346 agreement with the fluids to have equilibrated with their host rocks in a closed system with low  
347 fluid/rock ratios (Rolland and Rossi, 2016). In our study, observations of veins show that they were  
348 closely related to schistosity acting as a stylolitic dissolution surface (section 4.1). This observation is  
349 consistent with local fluid interactions and equilibrium with the host rock, resulting from a pressure-  
350 dissolution-recrystallization transfer mode (e.g. Passchier and Throw, 2005). Based on this, we suggest  
351 that the external fluid signature was buffered by the host rock signature. These fluid compositions  
352 show that ‘en-echelon’ veins are linked to an early deformation, where the porosity was still not  
353 connected by the fault network (Fig. 3). In such a system, the veins kept the host rock signature and no  
354 crustal-scale fluid flow circulation is evidenced.

355

356 *5.2. Scale of fluid flow in the brittle extensional structures*

357 Major (> metre-scale width) faults are related to shallower, or higher stress contexts (e.g. Passchier  
358 and Throw, 2005). The isotopic composition of calcite that crystallised in these brittle extensional  
359 faults is significantly different from their host rock (section 4.2; Fig. 6). Indeed, calcites related to  
360 these major faults have  $\delta^{18}\text{O}$  lower than 10 ‰ from their host rock and a  $\delta^{13}\text{C}$  ranging between -5 to 4  
361 ‰ PDB (while the  $\delta^{13}\text{C}$  ratio of Trias host rock is of 2 ‰). This signature is similar to that of  
362 exogenous metamorphic fluid origin (Crespo-Blanc et al., 1995; Rossi and Rolland, 2014). The  
363 observed CL pattern of calcites also argues for variations in the fluid composition, between the  
364 different veins and progressively within a given vein. Similar signatures are recorded in the Mont  
365 Blanc External Crystalline Massif shear zones and veins in a similar structural context (Rossi et al.,  
366 2014). There a similar spread of  $\delta^{13}\text{C}$ - $\delta^{18}\text{O}$  values is observed in the marginal part of the crystalline  
367 basement, at the contact with the Helvetic schists. This spread is interpreted as a mixing between  
368 fluids flowing down through the sedimentary cover and upwards fluids originating from shear zones in  
369 the Massif Central (Rolland and Rossi, 2016). The chemical signature of calcite veins in the Massif  
370 Central shear zones is correlated to a Mg-K-rich metasomatism, both arguing for  $\text{CO}_2$ -bearing fluids  
371 representative of a deep source, which is rooted in the mantle via vertical shear zones (Rossi et al.,  
372 2005). This deeply rooted fluid cell is also suggested by fluids significantly hotter (150-250 °C) than  
373 their host-rock at ca. 10 Ma along vertical faults in Belledonne Massif, which are in continuity with  
374 the central Mont Blanc Massif shear zones (Janots et al., 2019). Indeed, deep metamorphic fluid  
375 circulation is in good agreement with a crustal-scale fluid pathway which is activated during the  
376 extensional motion of the PFT, connected to the Rhône-Simplon right-lateral fault (Bergemann et al.,  
377 2019; 2020). This crustal-scale network suggests that extensional faults are in-depth connected to the  
378 PFT, when it was reactivated as a detachment. Deep connection with the PFT crustal scale structure  
379 (e.g. Sue et al., 2003) would allow fluid circulation from interface of European slab with the deep  
380 subduction/collisional metamorphosed prism. In our study, the isotopic dataset shows a significant  
381 difference between the deep fluids signature recorded by the Mont Blanc veins (Rossi and Rolland,  
382 2014; Rolland and Rossi, 2016) and the compositions of the veins related to brittle-ductile structures  
383 (Fig. 6). This variability suggests a mixing process between the local fluids trapped in the early  
384 extensional (closed system) and these exogenous fluids from a deep crustal origin.

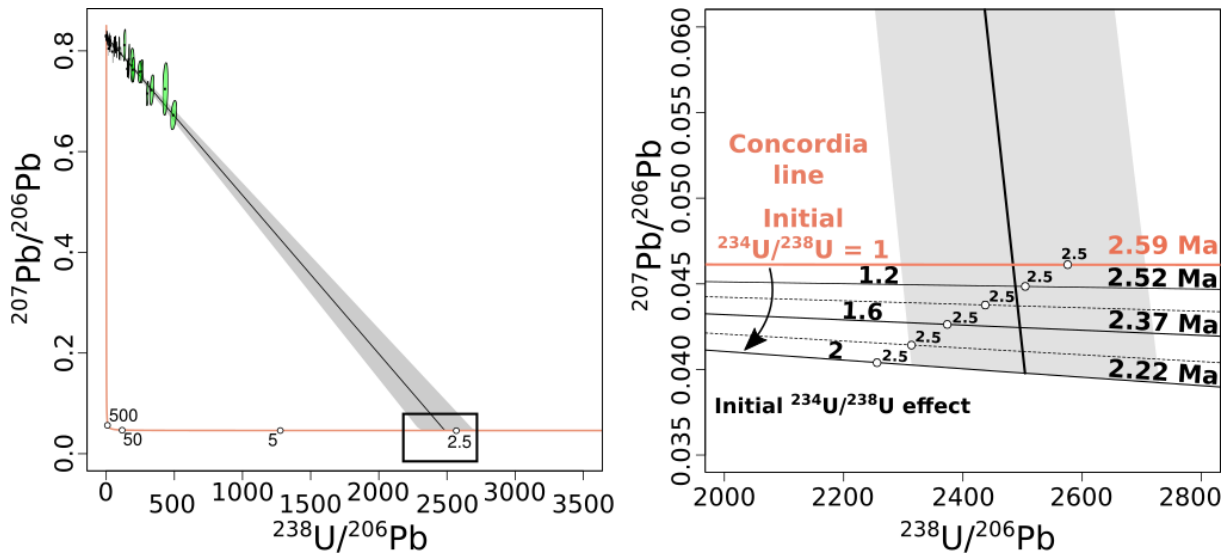
385

386 *5.3. Timing of PFT extensional inversion*

387 All ages obtained from the investigated Tournoux normal fault scarp, give direct time constraints on  
388 the final stages of extensional slip, and are interpreted as a minimum age for the extensional  
389 reactivation of the PFT. The oldest event is the formation of the highly deformed cataclasite calcite  
390 filling/veins  $\sim 3.5$  Ma ( $3.4 \pm 1.5$  Ma,  $3.6 \pm 0.4$  and  $3.4 \pm 0.6$ ). This calcitic cementation occurred directly

391 after the main cataclastic deformation event and before the late cross-cutting veins. Latter cross-  
392 cutting veins gave the same ~2.5 Ma age, with two within-error dates of  $2.6 \pm 0.3$  and  $2.3 \pm 0.3$  Ma. The  
393 ~3.5 Ma and ~2.5 Ma do not represent the same slip event on the fault. It is noteworthy that all these  
394 ages are calculated assuming secular equilibrium in the U-series decay chain. As fluids are generally  
395 characterized by an excess in  $^{234}\text{U}$  with respect to  $^{238}\text{U}$ , resulting in an excess of radiogenic  $^{206}\text{Pb}$ , the  
396 calculated ages should be considered as maximum ages (see for example Walker et al., 2006). The  
397 magnitude of the offset ages due to initial  $^{234}\text{U}/^{238}\text{U}$  disequilibrium can be significant and the true age  
398 could be younger by several hundreds of thousands of years. In the present case, it was not possible to  
399 carry out classical isotopic analyses of uranium by isotopic dilution to measure any detectable residual  
400  $^{234}\text{U}/^{238}\text{U}$  disequilibrium because of the size of the carbonate phases. It could be hazardous to speculate  
401 on the initial  $^{234}\text{U}/^{238}\text{U}$  disequilibria of the fluids, but the quite high uranium concentrations (up to the  
402 ppm level) observed in analysed minerals of samples FP-18-2 & 3 (Fig. 7) are likely indicative of an  
403 oxidizing environment and thus of a moderate initial  $^{234}\text{U}$  excess (Walker et al., 2006). To assess the  
404 impact of this excess on the final age, we have tested various initial  $^{234}\text{U}/^{238}\text{U}$  activity ratios ranging  
405 between 1 to 2 as illustrated in Figure 8. For an initial ( $^{234}\text{U}/^{238}\text{U}$ ) activity ratio of 2, the true age is  
406 lower by about ~370 ka. The obtained ages assuming an initial ( $^{234}\text{U}/^{238}\text{U}$ ) ratio of 1 are thus regarded  
407 as maximum ages.

408 As they remain undeformed, the latter veins are considered as the youngest tectonic slip along the  
409 fault. Furthermore, the geometry of the Tournoux normal fault regarding the PFT position indicates  
410 that this normal fault was connected to the PFT, which acted as a detachment Zone (Fig. 9). Thus, it  
411 may represent the paleo-HDFS seismogenic zone, which was later exhumed in the footwall part of the  
412 active extensional fault. Main activity of this paleo-fault can be bracketed between 3.4-2.2 Ma based  
413 on the above results.



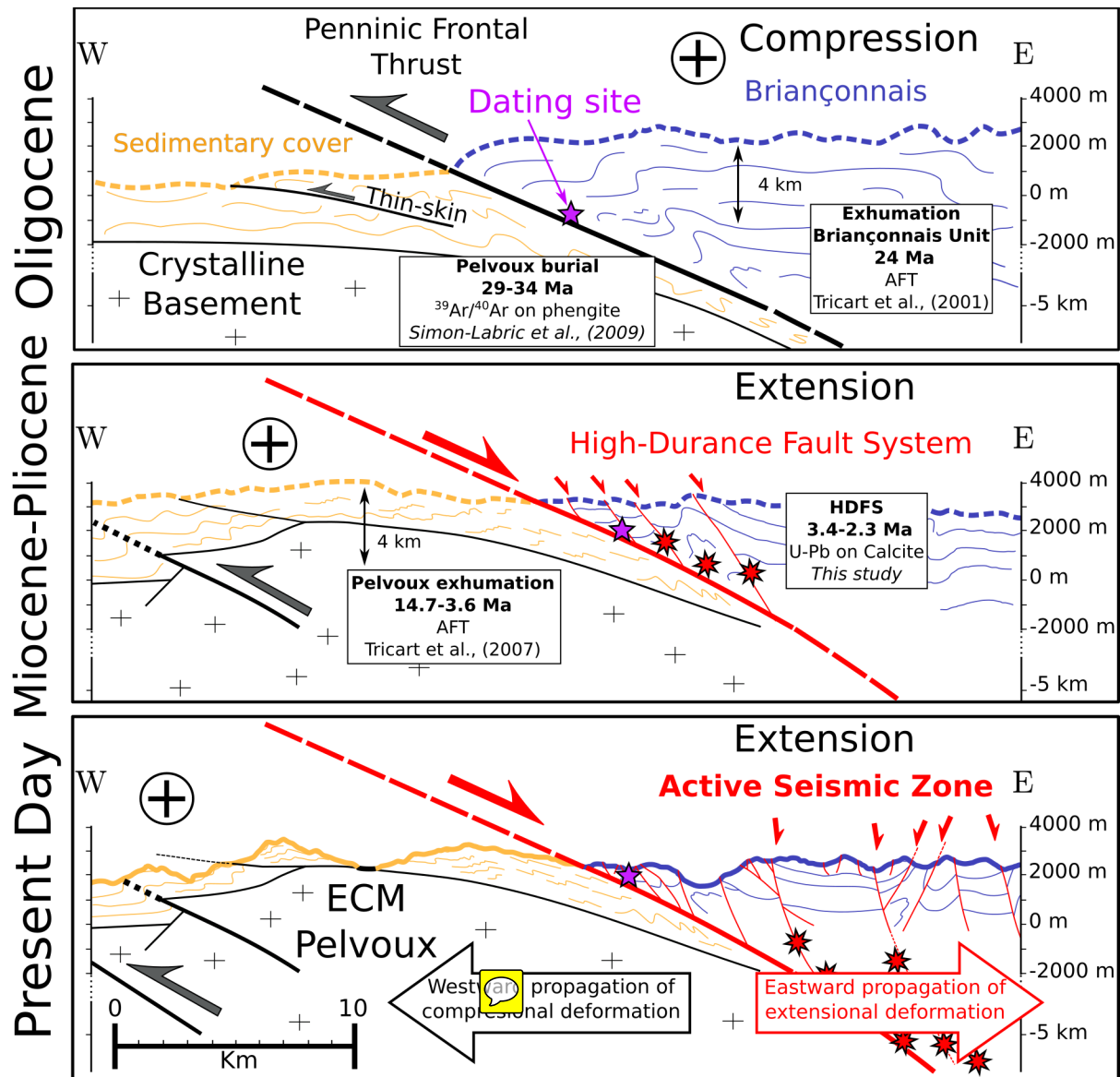
414 **Fig. 8.** Impact of the initial  $^{234}\text{U}$  excess on the final age estimation. Several initial  $^{234}\text{U}/^{238}\text{U}$  activity  
 415 ratios have been tested ranging between 1 to 2. This spread in initial  $^{234}\text{U}/^{238}\text{U}$  leads to an age  
 416 difference of 0.37 Ma. The obtained U/Pb age of 2.59 Ma, assuming equality of  $^{234}\text{U}$  and  $^{238}\text{U}$  contents  
 417 is thus a maximum age.

418

#### 419 5.4. Evolution of PFT through time

420 The structural and dating results presented in this paper, combined with the literature on PFT footwall  
 421 and hanging wall exhumation lead to the following reconstitution of its evolution (Fig. 9).

422 The investigated PFT paleoseismic zone is located 3 to 10 km west of the active HDFS seismogenic  
 423 zone. Nowadays, the extensional deformation is mainly localised on one active fault and mostly occurs  
 424 mostly at 3 to 8 km depth (Sue et al., 2007; Mathey et al., 2020). This study gives insights into the  
 425 uplift rate and lateral displacement of the High-Durance Fault System footwall and hanging wall since  
 426 the passage of the investigated paleo-PFT through the upper boundary of the seismogenic crust some  
 427 2-3.5 Ma ago. Since then, the PFT hanging wall, represented by the active extensional deformation  
 428 front of the HDFS was significantly shifted eastward, while its footwall was uplifted up to 3 km (Fig.  
 429 9). This leads to a mean vertical tectonic motion on the order of  $> 1 \text{ mm.yr}^{-1}$  for the footwall  
 430 compartment of PFT on this period of time. This rate is consistent with the vertical GPS rates  
 431 measured for the Pelvoux External Crystalline Massif (Nocquet et al., 2016; Sternai et al., 2019).



432 Fig. 9. Evolutionary geological cross-section sketch of PFT (modified from Tricart et al., 2006). **a**,  
 433 **Compressional** activation of the PFT resulting in joint External Crystalline Massifs burial and Briançonnais  
 434 exhumation during the Oligocene. **b**, Extensional reactivation of the PFT and setting up of the High-Durance  
 435 Fault System during the Pliocene as evidenced in this study. At this point the dated extensional fault passes  
 436 through the upper boundary of the seismic zone at ca. 2-3 Ma. **c**, At present-day, **compressional** deformation has  
 437 migrated westward (frontal part of External Crystalline Massifs, since c. 15 Ma) and extensional seismic activity  
 438 of the High-Durance Fault System is recorded at shallow depth 3-10 km east of the studied paleoseismic zone.

439

440 Our data support the hypothesis that the present HDFS is the result of eastward shifting of extensional  
 441 deformation, accommodated by successive jumps on several faults. Faults were likely active on a scale  
 442 of  $\geq 1$  Myr before becoming inactive. Calcite U-Pb ages obtained on the Tournoux scarp constrain co-  
 443 seismic motion on two conjugate faults. The two age groups obtained on these extensional faults  
 444 connected to the PFT highlight at least two phases of deformation, at  $3.5 \pm 0.4$  Ma and one or two

445 discrete brittle events at, or comprised within,  $2.6\pm 0.2$  and  $2.3\pm 0.2$  Ma, which gives insights into the  
446 long-term activity of the of at least 1 Myr, but with only several datable events, which argues for an  
447 apparent contradiction. Indeed, co-seismic displacement on the fault suggest a significant magnitude  
448 for the related earthquake (Wells and Coppersmith, 1994), which is apparently incompatible with the  
449 very few datable motions. This gives some weight to a deformation regime which may alternate phase  
450 of creeping on the fault plane, without any brittle deformation, with very rare phases of brittle  
451 deformation.

452 The vertical uplift and exhumation of the Pelvoux External Massif since 3.5 Ma may thus mainly  
453 result from the cumulated fault motion on these several fault segments. These data are thus in  
454 agreement with a significant tectonic component in the measured uplift signal of External Crystalline  
455 Massifs, which is in agreement with a clear difference in uplift rates measured between ECMs and  
456 Internal Alps (Nocquet et al., 2016; Sternai et al., 2019).

457 We support the hypothesis that the HDFS is the result of the eastward extensional deformation shift  
458 and the successive formation of younger faults normal fault participated at the exhumation of the  
459 directly to the west block.

460

## 461 **6. Conclusion**

462 Significant constraints on the evolution of fault systems can be acquired by coupling stable isotopic  
463 analysis and U-Pb dating on calcite. These methods have been successfully applied to unravel the  
464 tectonic reactivation of the PFT for the first time. Five U-Pb ages on calcite have been obtained on  
465 extensional fault structures connected to the PFT, gave two distinct group of ages of  $3.5\pm 0.5$  Ma for  
466 the main deformation phase represented by the cataclasite calcite cement, cross-cut by later discrete  
467 phases represented by mm-large veins dated from  $2.6\pm 0.3$  to  $2.3\pm 0.3$  Ma. The 3.5 Ma age represents a  
468 minimum age for the onset of extensional brittle reactivation of the PFT. Earliest extensional ductile-  
469 brittle structures cannot be dated due to low uranium contents and low U/Pb ratios. Associated to those  
470 two (ductile and brittle) deformation stages, stable isotopic ratios of carbon ( $\delta^{13}\text{C}$ ) and oxygen ( $\delta^{18}\text{O}$ )  
471 of calcite samples collected within the kilometre-scale extensional faults show an evolution from a  
472 closed to an open fluid system. The isotopic signature of fluids related to the brittle deformation stage  
473 corresponds an open system due to the activation of a crustal-scale fluid circulation cell when the  
474 HDFS developed in connection with the deeper PFT deeper structure. The fluids associated to this  
475 open system show a deep crustal/mantle signature similar to that measured along the PFT across the  
476 Alpine arc. This deeply rooted upward fluid circulation occurred when extensional fault activity was  
477 connected to the PFT reactivated as a detachment, which suggests a crustal-scale extensional  
478 reactivation at this stage. These constraints on PFT fluid regime are the first direct evidence for a  
479 transition towards a crustal-scale fluid regime at the onset of brittle extensional reactivation in the

480 Alps. The direct ages of PFT motion give insights into the long-term incremental displacement of the  
481 HDFS footwall, and Pelvoux Massif exhumation, which corresponds to its passage through the upper  
482 part of the seismogenic zone, at a mean rate of  $> 1 \text{ mm.yr}^{-1}$  in the last 3 Ma.

483

#### 484 **Acknowledgements**

485 This work forms part of first author's Ph.D. funded by the BRGM in the frame of the RGF project.  
486 The CEREGE group is supported by 2 French "Investissements d'Avenir" fundings: the EQUIPEX-  
487 ASTER-CEREGE and the Initiative d'Excellence of Aix-Marseille University - A\*Midex, through the  
488 DatCarb project. We wish to thank Fayçal Soufi for his help in sample preparation.

489

#### 490 **Author contributions**

491 AB, YR and SS wrote the manuscript and all authors discussed the results and contributed to the final  
492 article. TD supported AB for map creation and cross-sections. YR, SS, TD, CG and AB participated to  
493 field trip sampling. AB did the sample petrographic characterization with optical microscope and  
494 cathodoluminescence. NG, AG and PD led U-Pb dating with AB. BB and AN supervised AB for stable  
495 isotopes analysis, for results interpretation and protocol application respectively.

496

#### 497 **Supplementary Materials**

498 Suppl. Mat. Table S1. Sample locations and descriptions.

499 Suppl. Mat. Fig. S1. Tournoux's scarp general view.

500 Suppl. Mat. Fig. S2. Field photographs FP19-12 site.

501 Suppl. Mat. Fig. S3. La-ICPMS elemental maps, FP18-2B.

502 Suppl. Mat. Fig. S4. FP19-12B thin section with map localisation.

503 Suppl. Mat. Fig. S5. La-ICPMS elemental map, FP19-12B.

504

505 Suppl. Mat. Table S2. U-Pb on calcite La-ICPMS data.

506

**Table 1: Isotopic composition of analysed calcites**

	N°Sample	<sup>13</sup> δC PDB	<sup>18</sup> δO SMOW	
<i>Whole Rock</i>	FP18-1A	2,15	17,18	
	FP18-1A	2,09	16,90	
	FP18-4	1,92	24,83	
	FP18-7	2,25	25,76	
	FP18-9	-0,32	22,00	
	FP18-10	1,26	28,59	
	FP18-11	2,1	26,51	
	FP18-13	3,43	23,73	
	<i>Early veins (V1)</i>	FP18-1B	2,59	19,89
		FP18-1C	2,48	20,74
		FP18-1C	2,48	18,84
FP18-9		-0,18	22,59	
FP18-10		1,29	28,99	
FP18-11		1,58	23,37	
<i>En-echelon veins (V2)</i>	FP18-1A	2,12	17,65	
	FP18-1A	2,18	18,15	
	FP18-1B	1,96	17,71	
	FP18-1D	1,88	17,98	
	FP18-5	1,66	25,80	
	<i>Cataclasite infill (V2)</i>	FP18-2A	0,03	7,43
FP18-2B		-0,09	7,86	
FP18-3B		-4,62	11,41	
FP18-3B		-0,75	12,10	
FP18-6		-3,04	10,23	
FP18-6		-0,95	12,68	
FP18-13		3,46	13,29	
FP18-13		2,53	14,38	
FP18-13		3,4	7,21	

**Table 1.** Stable isotope data, first bloc for host rock, second bloc compressive veins, third early small scale extensional features, fourth main large scale extensional features.

507  
508  
509  
510

511 **Références**

- 512 Andrieu, S., Brigaud, B., Rabourg, T., and Noret, A.: The Mid-Cenomanian Event in shallow marine  
513 environments: Influence on carbonate producers and depositional sequences (northern Aquitaine  
514 Basin, France), *Cretaceous Res.*, 56, 587–607, <https://doi.org/10.1016/j.cretres.2015.06.018>, 2015.
- 515 Ault, A. K., Gautheron, C., and King, G. E.: Innovations in (U–Th)/He, fission track, and trapped  
516 charge thermochronometry with applications to earthquakes, weathering, surface-mantle  
517 connections, and the growth and decay of mountains, *Tectonics*, 38(11), 3705–3739,  
518 <https://doi.org/10.2029/2018TC005312>, 2019.
- 519 Barnaby, R. J. and Rimstidt, J. D.: Redox conditions of calcite cementation interpreted from Mn and  
520 Fe contents of authigenic calcites, *Geol. Soc. Am. Bull.*, 101(6), 795–804,  
521 [https://doi.org/10.1130/0016-7606\(1989\)101<0795:RCOCCI>2.3.CO;2](https://doi.org/10.1130/0016-7606(1989)101<0795:RCOCCI>2.3.CO;2), 1989.
- 522 Beaudoin, N., Huyghe, D., Bellahsen, N., Lacombe, O., Emmanuel, L., Mouthereau, F., and  
523 Ouahnon, L.: Fluid systems and fracture development during syn-depositional fold growth: An  
524 example from the Pico del Aguila anticline, Sierras Exteriores, southern Pyrenees, Spain. *J. Struct.*  
525 *Geol.*, 70, 23–38, <https://doi.org/10.1016/j.jsg.2014.11.003>, 2015.
- 526 Beaudoin, N., Lacombe, O., Roberts, N.M.W., and Koehn, D.: U-Pb dating of calcite veins reveals  
527 complex stress evolution and thrust sequence in the Bighorn Basin, Wyoming, USA. *Geology*, 46,  
528 1015–1018, <https://doi.org/10.1130/G45379.1>, 2018.
- 529 Bellahsen, N., Mouthereau, F., Boutoux, A., Bellanger, M., Lacombe, O., Jolivet, L., and Rolland, Y.:  
530 Collision kinematics in the western external Alps, *Tectonics*, 33(6), 1055–1088,  
531 <https://doi.org/10.1002/2013TC003453>, 2014.
- 532 Bellanger, M., Augier, R., Bellahsen, N., Jolivet, L., Monié, P., Baudin, T., and Beyssac, O.:  
533 Shortening of the European Dauphinois margin (Oisans Massif, Western Alps): New insights from  
534 RSCM maximum temperature estimates and  $^{40}\text{Ar}/^{39}\text{Ar}$  in situ dating, *J. Geodyn.*, 83, 37–64,  
535 <https://doi.org/10.1016/j.jog.2014.09.004>, 2015.
- 536 Beltrando, M., Lister, G.S., Forster, M., Dunlap, W.J., Fraser, G., and Hermann, J.: Dating  
537 microstructures by the  $^{40}\text{Ar}/^{39}\text{Ar}$  step-heating technique: Deformation–pressure–temperature–time  
538 history of the Penninic Units of the Western Alps, *Lithos*, 113, 801–819,  
539 <https://doi.org/10.1016/j.lithos.2009.07.006>, 2009.
- 540 Bergemann, C.A., Gnos, E., and Whitehouse, M.J.: Insights into the tectonic history of the Western  
541 Alps through dating of fissure monazite in the Mont Blanc and Aiguilles Rouges Massifs,  
542 *Tectonophysics*, 750, 203–212, <https://doi.org/10.1016/j.tecto.2018.11.013>, 2019.
- 543 Bergemann, C.A., Gnos, E., Berger, A., Janots, E., and Whitehouse, M.J.: Dating tectonic activity in  
544 the Lepontine Dome and Rhone-Simplon Fault regions through hydrothermal monazite-(Ce), *Solid*  
545 *Earth*, 11, 199–222, <https://doi.org/10.5194/se-11-199-2020>, 2020.
- 546 Bertrand, A. and Sue, C.: Reconciling late faulting over the whole Alpine belt: from structural analysis  
547 to geochronological constrains, *Swiss J. Geosci.*, 110, 565–580, [https://doi.org/10.1007/s00015-](https://doi.org/10.1007/s00015-017-0265-4)  
548 [017-0265-4](https://doi.org/10.1007/s00015-017-0265-4), 2017.

549 Beucher, R., van der Beek, P., Braun, J., and Batt, G.E.: Exhumation and relief development in the  
550 Pelvoux and Dora-Maira analysis and inversion of thermochronological age transects, *J. Geophys.*  
551 *Res.*, 117, F03030, <https://doi.org/10.1029/2011JF002240>, 2012.

552 Bons, P.D., Elburg, M.A., and Gomez-Rivas, E.: A review of the formation of tectonic veins and their  
553 microstructures, *J. Struct. Geol.*, 43, 33–62. <https://doi.org/10.1016/j.jsg.2012.07.005>, 2012.

554 Boutoux, A., Bellahsen, N., Nanni, U., Pik, R., Verlaquet, A., Rolland, Y., and Lacombe, O.: Thermal  
555 and structural evolution of the external Western Alps: Insights from (U–Th–Sm)/He  
556 thermochronology and RSCM thermometry in the Aiguilles Rouges/Mont Blanc massifs,  
557 *Tectonophysics*, 683, 109–123, <https://doi.org/10.1016/j.tecto.2016.06.010>, 2016.

558 Cederbom, C.E., Sinclair, H.D., Schlunegger, F., and Rahn, M.K.: Climate induced rebound and  
559 exhumation of European Alps, *Geology*, 32, 709–712, <https://doi.org/10.1130/G20491.1>, 2004.

560 Cenki-Tok, B., Darling, J.R., Rolland, Y., Dhuime, B., and Storey, C.D.: Direct dating of mid-crustal  
561 shear zones with synkinematic allanite: new in situ U-Th-Pb geochronological approaches applied  
562 to the Mont Blanc massif, *Terra Nova*, 26, 29–37, <https://doi.org/10.1111/ter.12066>, 2014.

563 Ceriani, S., Fügenschuh, B., and Schmid, S. M.: Multi-stage thrusting at the " Penninic Front" in the  
564 Western Alps between Mont Blanc and Pelvoux massifs, *Int. J. Earth Sci.*, 90(3), 685-702,  
565 <https://doi.org/10.1007/s005310000188>, 2001.

566 Ceriani, S. and Schmid, S.M.: From N-S collision to WNW-directed post-collisional thrusting and  
567 folding: Structural study of the Frontal Penninic Units in Savoie (Western Alps, France), *Eclogae*  
568 *geol. Helv.*, 97, 347–369, <https://doi.org/10.1007/s00015-004-1129-2>, 2004.

569 Champagnac, J. D., Molnar, P., Anderson, R. S., Sue, C., and Delacou, B.: Quaternary erosion-induced  
570 isostatic rebound in the western Alps, *Geology*, 35(3), 195-198, <https://doi.org/10.1130/G23053A.1>,  
571 2007.

572 Crespo-Blanc, A., Masson, H., Sharp, Z., and Cosca, M.: A stable and  $^{40}\text{Ar}/^{39}\text{Ar}$  isotope study of a  
573 major thrust in the Helvetic nappes (Swiss Alps): Evidence for fluid flow and constraints on nappe  
574 kinematics, *Geol. Soc. Am. Bull.*, 107(10), 1129-1144, [https://doi.org/10.1130/0016-  
575 7606\(1995\)107<1129:ASAAAI>2.3.CO;2](https://doi.org/10.1130/0016-7606(1995)107<1129:ASAAAI>2.3.CO;2), 1995.

576 Duchêne, S., Blichert-Toft, J., Luais, B., Télouk, P., Lardeaux, J.-M., and Albarède, F.: The Lu–Hf  
577 dating of garnets and the ages of the Alpine high-pressure metamorphism, *Nature*, 387, 586–589,  
578 <https://doi.org/10.1038/42446>, 1997.

579 Dumont, T., Schwartz, S., Guillot, S., Simon-Labric, T., Tricart, P., and Jourdan, S.: Structural and  
580 sedimentary records of the Oligocene revolution in the Western Alpine arc, *J. Geodyn.*, 56–57, 18–  
581 38, <https://doi.org/10.1016/j.jog.2011.11.006>, 2012.

582 Goodfellow, B.W., Viola, G., Bingen, B., Nuriel, P., and Kylander-Clark, A.R.C.: Palaeocene faulting  
583 in SE Sweden from U-Pb dating of slickenfibres calcite, *Terra Nova*, 29, 321–328,  
584 <https://doi.org/10.1111/ter.12280>, 2017.

585 Janots, E., Grand'Homme, A., Bernet, M., Guillaume, D., Gnos, E., Boiron, M. C., Rossi, M.,  
586 Seydoux-Guillaume, A.-M., and De Ascensão Guedes, R.: Geochronological and thermometric

587 evidence of unusually hot fluids in an Alpine fissure of Lauzière granite (Belledonne, Western  
588 Alps), *Solid Earth*, 10(1), 211-223, <https://doi.org/10.5194/se-10-211-2019>, 2019.

589 Jochum, K. P., Weis, U., Stoll, B., Kuzmin, D., Yang, Q., Raczek, I., Jacob, D.E., Stracke, A.,  
590 Birbaum, K., Frick, D.A., Günther, D., and Enzweiler, J.: Determination of reference values for  
591 NIST SRM 610–617 glasses following ISO guidelines, *Geostand. Geoanal. Res.*, 35(4), 397-429.  
592 <https://doi.org/10.1111/j.1751-908X.2011.00120.x>, 2011.

593 Kim, S.-T., Coplen, T.B., and Horita, J.: Normalization of stable isotope data for carbonate minerals:  
594 Implementation of IUPAC guidelines, *Geochim. Cosmochim. Ac.*, 158, 276–289,  
595 <https://doi.org/10.1016/j.gca.2015.02.011>, 2015.

596 Lanari, P., Guillot, S., Schwartz, S., Vidal, O., Tricart, P., Riel, N., and Beyssac, O.: Diachronous  
597 evolution of the alpine continental wedge: evidences from P-T estimates in the Briançonnais Zone  
598 houillère (France-Western Alps), *J. Geodyn.*, 56-57, 39–54,  
599 <https://doi.org/10.1016/j.jog.2011.09.006>, 2012.

600 Lanari, P., Rolland, Y., Schwartz, S., Vidal, O., Guillot, S., Tricart, P., and Dumont, T.: P-T-t estimation  
601 of syn-kinematic strain in low-grade rocks (<300°C) using thermodynamic modelling and <sup>40</sup>Ar/<sup>39</sup>Ar  
602 dating techniques: example of the Plan-de-Phasy shear zone (Briançonnais Zone, Western Alps),  
603 *Terra Nova*, 26, 130–138, <https://doi.org/10.1111/ter.12079>, 2014.

604 Lardeaux J.M., Schwartz S., Tricart P., Paul A., Guillot S., Béthoux N., and Masson F.: A crustal-scale  
605 cross-section of the southwestern Alps combining geophysical and geological imagery, *Terra Nova*,  
606 18 (6), 412-422, <https://doi.org/10.1111/j.1365-3121.2006.00706.x>, 2006.

607 Larroque, C., Delouis, B., Godel, B., and Nocquet, J.-M.: Active deformation at the southwestern  
608 Alps–Ligurian basin junction (France–Italy boundary): Evidence for recent change from  
609 compression to extension in the Argentera massif, *Tectonophysics*, 467, 22–34,  
610 <https://doi.org/10.1016/j.tecto.2008.12.013>, 2009.

611 Malusà, M., Zhao, L., Eva, E., Solarino, S., Paul, A., Guillot, S., Schwartz, S., Dumont, T., Aubert, C.,  
612 Salimbeni, S., Pondrelli, S., Wang, and Q., Zhu, R.: Earthquakes in the western alpine mantle  
613 wedge, *Gondwana Research*, 44, 89-95, <http://dx.doi.org/10.1016/j.gr.2016.11.012>, 2017.

614 Mathey, M., Walpersdorf, A., Sue, C., Baize, S., and Deprez, A.: Seismogenic potential of the High  
615 Durance Fault constrained by 20 yr of GNSS measurements in the Western European Alps,  
616 *Geophy. J. Int.*, 222(3), 2136-2146, <https://doi.org/10.1093/gji/ggaa292>, 2020.

617 Mugnier, J. L., Loubat, H., and Cannic, S.: Correlation of seismic images and geology at the boundary  
618 between internal and external domains of the Western Alps, *Bull. Soc. Géol. Fr.*, 164(5), 697-708,  
619 1993.

620 Nardini, N., Muñoz-López, D., Cruset, D., Cantarero, I., Martín-Martín, J., Benedicto, A., Gomez-  
621 Rivas, E., John, C., and Travé, A.: From Early Contraction to Post-Folding Fluid Evolution in the  
622 Frontal Part of the Bóixols Thrust Sheet (Southern Pyrenees) as Revealed by the Texture and  
623 Geochemistry of Calcite Cements, *Minerals*, 9, 117, <https://doi.org/10.3390/min9020117>, 2019.

624 Nocquet, J. M., Sue, C., Walpersdorf, A., Tran, T., Lenôtre, N., Vernant, P., Cushing, M., Jouanne, F.,  
625 Masson, F., Baize, S., Chéry, J., and Van der Beek, P. A.: Present-day uplift of the western Alps,  
626 *Sci. Rep.*, 6(1), 1-6, <https://doi.org/10.1038/srep28404>, 2016.

627 Passchier, C.W. and Trouw, R.A.J.: *Microtectonics*, 2<sup>nd</sup> rev. ed. Springer, Berlin, New York, 2005.

628 Paton, C., Hellstrom, J., Paul, B., Woodhead, J., and Hergt, J.: Iolite: Freeware for the visualisation  
629 and processing of mass spectrometric data, *J. Anal. Atom. Spectrom.*, 26(12), 2508-2518,  
630 <https://doi/10.1039/c1ja10172b>, 2011.

631 Ring, U. and Gerdes, A.: Kinematics of the Alpenrhein-Bodensee graben system in the Central Alps:  
632 Oligocene/Miocene transtension due to formation of the Western Alps arc, *Tectonics*, 35(6), 1367-  
633 1391, <https://doi.org/10.1002/2015TC004085>, 2016.

634 Roberts, N.M.W., Rasbury, E.T., Parrish, R.R., Smith, C.J., Horstwood, M.S.A., and Condon, D.J.: A  
635 calcite reference material for LA-ICP-MS U-Pb geochronology: Calcite RM for LA-ICP-MS U-Pb  
636 dating, *Geochem. Geophys. Geosyst.*, 18, 2807–2814, <https://doi.org/10.1002/2016GC006784>,  
637 2017.

638 Roberts, N.M.W., Drost, K., Horstwood, M.S.A., Condon, D.J., Chew, D., Drake, H., Milodowski,  
639 A.E., McLean, N.M., Smye, A.J., Walker, R.J., Haslam, R., Hodson, K., Imber, J., and Beaudoin,  
640 N.: LA-ICP-MS U-Pb carbonate geochronology: strategies, progress, and application to fracture-  
641 fill calcite, *Geochronology*, <https://doi.org/10.5194/gchron-2019-15>, 2020.

642 Rolland, Y., Rossi, M., Cox, S. F., Corsini, M., Mancktelow, N., Pennacchioni, G., Fronari, M., and  
643 Boullier, A.M.: <sup>40</sup>Ar/<sup>39</sup>Ar dating of synkinematic white mica: insights from fluid-rock reaction in  
644 low-grade shear zones (Mont Blanc Massif) and constraints on timing of deformation in the NW  
645 external Alps, *Geological Society, London, Special Publications*, 299(1), 293-315,  
646 <https://doi.org/10.1144/SP299.18>, 2008.

647 Rolland, Y. and Rossi, M.: Two-stage fluid flow and element transfers in shear zones during collision  
648 burial-exhumation cycle: Insights from the Mont Blanc Crystalline Massif (Western Alps), *J.*  
649 *Geodyn.*, 101, 88-108, <https://doi.org/10.1016/j.jog.2016.03.016>, 2016.

650 Rossi, M., Rolland, Y., Vidal, O., and Cox, S.F.: Geochemical variations and element transfer during  
651 shear-zone development and related episyenites at middle crust depths: insights from the Mont  
652 Blanc granite (French-Italian Alps), *Geological Society, London, Special Publications*, 245, 373–  
653 396, <https://doi.org/10.1144/GSL.SP.2005.245.01.18>, 2005.

654 Rossi, M. and Rolland, Y.: Stable isotope and Ar/Ar evidence of prolonged multiscale fluid flow  
655 during exhumation of orogenic crust: Example from the Mont Blanc and Aar Massifs (NW Alps):  
656 Multi-scale fluid flow in the Alps, *Tectonics*, 33, 1681–1709,  
657 <https://doi.org/10.1002/2013TC003438>, 2014.

658 Rothé, E.: *La sismicité des Alpes occidentales. Annales de l'Institut de Physique du Globe de*  
659 *Strasbourg*, III, 1941.

660 Rubatto, D. and Hermann, J.: Zircon formation during fluid circulation in eclogites (Monviso, Western  
661 Alps): implications for Zr and Hf budget in subduction zones, *Geochim. et Cosmochim. Ac.*, 67,  
662 2173–2187, [https://doi.org/10.1016/S0016-7037\(02\)01321-2](https://doi.org/10.1016/S0016-7037(02)01321-2), 2003.

663 Salimbeni, S., Zhao, L., Malusà, M., Guillot, S., Pondrelli, S., Margheriti, L., Paul, A., Solarino, S.,  
664 Aubert, C., Dumont, T., Schwartz, S., Wang, Q., Xu, X., Zheng, T., and Zhu, R.: Fossil and active  
665 mantle flows in the western Alpine region unravelled by seismic anisotropy analysis and high-  
666 resolution P wave tomography, *Tectonophysics*, 731-732, 35–47,  
667 <https://doi.org/10.1016/j.tecto.2018.03.002>, 2018.

668 Sanchez, G., Rolland, Y., Schneider, J., Corsini, M., Oliot, E., Goncalves, P., Verati, C., Lardeaux, J.-  
669 M., and Marquer D.: Dating low-temperature deformation by  $^{40}\text{Ar}/^{39}\text{Ar}$  on white mica, insights  
670 from the Argentera-Mercantour Massif (SW Alps), *Lithos*, 125(1-2), 521-536,  
671 <https://doi.org/10.1016/j.lithos.2011.03.009>, 2011.

672 Seward, D. and Mancktelow, N.S.: Neogene kinematics of the central and western Alps: Evidence  
673 from fission-track dating, *Geology*, 22(9), 803-806, [https://doi.org/10.1130/0091-  
674 7613\(1994\)022<0803:NKOTCA>2.3.CO;2](https://doi.org/10.1130/0091-7613(1994)022<0803:NKOTCA>2.3.CO;2), 1994.

675 Schmid, S.M. and Kissling, E.: The arc of the western Alps in the light of geophysical data on deep  
676 crustal structure, *Tectonics*, 19, 62–85, <https://doi.org/10.1029/1999TC900057>, 2000.

677 Schwartz, S., Lardeaux, J.M., Tricart, P., Guillot, S., and Labrin, E.: Diachronous exhumation of HP-  
678 LT metamorphic rocks from south-western Alps: evidence from fission-track analysis, *Terra Nova*,  
679 19, 133–140, <https://doi.org/10.1111/j.1365-3121.2006.00728.x>, 2007.

680 Schwartz, S., Gautheron, C., Audin, L., Dumont, T., Nomade, J., Barbarand, J., Pinna-Jamme, R., and  
681 van der Beek, P.: Foreland exhumation controlled by crustal thickening in the Western Alps,  
682 *Geology*, 45, 139-142, <https://doi.org/10.1130/G38561.1>, 2017.

683 Simon-Labric, T., Rolland, Y., Dumont, T., Heymes, T., Authemayou, C., Corsini, M., and Fornari, M.:  
684  $^{40}\text{Ar}/^{39}\text{Ar}$  dating of Penninic Front tectonic displacement (W Alps) during the Lower Oligocene (31-  
685 34 Ma), *Terra Nova*, 21, 127–136, <https://doi.org/10.1111/j.1365-3121.2009.00865.x>, 2009.

686 Smeraglia, L., Fabbri, O., Choulet, F., Buatier, M., Boulvais, P., Bernasconi, S.M., and Castorina, F.:  
687 Syntectonic fluid flow and deformation mechanisms within the frontal thrust of a foreland fold-  
688 and-thrust belt: Example from the Internal Jura, Eastern France, *Tectonophysics*, 778, 228178.  
689 <https://doi.org/10.1016/j.tecto.2019.228178>, 2020.

690 Sternai, P., Sue, C., Husson, L., Serpelloni, E., Becker, T.W., Willett, S.D., Faccenna, C., Di Giulio, A.,  
691 Spada, G., Jolivet, L., Valla, P., Petit, C., Nocquet, J.-M., Walpersdorf, A., and Castelltort, S.:  
692 Present-day uplift of the European Alps: Evaluating mechanisms and models of their relative  
693 contributions, *Earth-Sci. Rev.*, 190, 589–604, <https://doi.org/10.1016/j.earscirev.2019.01.005>, 2019.

694 Sue, C. and Tricart, P.: Late Alpine brittle extension above the Frontal Pennine Thrust near Briançon,  
695 Western Alps, *Eclogae Geol. Helv.*, 92(2), 171-181, <https://doi.org/10.5169/SEALS-168659>, 1999.

696 Sue, C. and Tricart, P.: Neogene to ongoing normal faulting in the inner western Alps: a major  
697 evolution of the alpine tectonics, *Tectonics*, 22, 1–25, <https://doi.org/10.1029/2002TC001426>,  
698 2003.

699 Sue, C., Delacou, B., Champagnac, J.-D., Allanic, C., Tricart, P., and Burkhard, M.: Extensional  
700 neotectonics around the bend of the Western/Central Alps: an overview, *Int. J. Earth Sci. (Geol  
701 Rundsch)*, 96, 1101–1129, <https://doi.org/10.1007/s00531-007-0181-3>, 2007.

702 Sue, C., Thouvenot, F., Fréchet, J., and Tricart, P.: Widespread extension in the core of the western  
703 Alps revealed by earthquake analysis, *J. Geophys. Res.-Sol. Ea.*, 104(B11), 25611-25622,  
704 <https://doi.org/10.1029/1999JB900249>, 1999.

705 Tardy, M., Deville, E., Fudral, S. E. R. E., Guellec, S., Ménard, G., Thouvenot, F., and Vialon, P.:  
706 Interprétation structurale des données du profil de sismique réflexion profonde ECORS-CROP  
707 Alpes entre le front Pennique et la ligne du Canavese (Alpes occidentales), *Mém. S. Géol. F.*, 156,  
708 217-226, 1990.

709 Thouvenot, F., Fréchet, J., Pinter, N., Gyula, G., Weber, J., Stein, S., and Medak, D. (Eds.): Seismicity  
710 along the northwestern edge of the Adria Microplate, *The Adria Microplate: GPS Geodesy,  
711 Tectonics and Hazards*, Nato Si. S. IV Ear. En. Kluwer Academic Publishers, Dordrecht, 335–349.  
712 [https://doi.org/10.1007/1-4020-4235-3\\_23](https://doi.org/10.1007/1-4020-4235-3_23), 2006.

713 Tricart, P.: From passive margin to continental collision; a tectonic scenario for the Western Alps, *Am.  
714 J. Sci.*, 284(2), 97-120, <https://doi.org/10.2475/ajs.284.2.97>, 1984.

715 Tricart, P., Schwartz, S., Sue, C., Poupeau, G., and Lardeaux, J.-M.: La dénudation tectonique de la  
716 zone ultradauphinoise et l'inversion du front briançonnais au sud-est du Pelvoux (Alpes  
717 occidentales); une dynamique miocène à actuelle, *B. Soc. Geol. Fr.*, 172(1), 49-58,  
718 <https://doi.org/10.2113/172.1.49>, 2001.

719 Tricart, P., Lardeaux, J.-M., Schwartz, S., and Sue, C.: The late extension in the inner western Alps: a  
720 synthesis along the south-Pelvoux transect, *B. Soc. Geol. Fr.*, 177, 299–310,  
721 <https://doi.org/10.2113/gssgfbull.177.6.299>, 2006.

722 Tricart, P., Van Der Beek, P., Schwartz, S., and Labrin, E.: Diachronous late-stage exhumation across  
723 the western Alpine arc: constraints from apatite fission-track thermochronology between the  
724 Pelvoux and Dora-Maira Massifs, *J. Geol. Soc.*, 164, 163–174, [https://doi.org/10.1144/0016-  
725 76492005-174](https://doi.org/10.1144/0016-76492005-174), 2007.

726 Vermeesch, P.: IsoplotR: A free and open toolbox for geochronology, *Geosci. Front.*, 9(5), 1479-1493,  
727 <https://doi.org/10.1016/j.gsf.2018.04.001>, 2018.

728 Walker, J., Cliff, R.A., and Latham, A.G.: U-Pb isotopic age of the StW 573 hominid from  
729 Sterkfontein, South Africa. *Science*, 314(5805), 1592-1594, <https://doi/10.1126/science.1132916>,  
730 2006.

731 Walpersdorf, A., Pinget, L., Vernant, P., Sue, C., Deprez, A., and the RENAG team.: Does Long-Term  
732 GPS in the Western Alps Finally Confirm Earthquake Mechanisms? , *Tectonics*, 37, 3721–3737.  
733 <https://doi.org/10.1029/2018TC005054>, 2018.

734 Wells, D. L., and Coppersmith, K. J.: New empirical relationships among magnitude, rupture length,  
735 rupture width, rupture area, and surface displacement, *Bull. Seismol. Soc. Am.*, 84(4), 974-1002,  
736 1994.

737 Woodhead, J.D. and Hergt, J.M.: Strontium, Neodymium and Lead Isotope Analyses of NIST Glass  
738 Certified Reference Materials: SRM 610, 612, 614, *Geostand. Geoanal. Res.*, 25, 261–266,  
739 <https://doi.org/10.1111/j.1751-908X.2001.tb00601.x>, 2001.

740 Zhao, L., Paul A., Solarino S., Guillot S., Malusà M., Zheng T., Aubert C., Salimbeni S., Dumont T.,  
741 Schwartz S., Pondrelli S., Zhu R., and Wang Q. First seismic evidence for continental subduction  
742 beneath the Western Alps, *Geology*, 43, 815-818, <https://doi.org/10.1130/G36833.1>, 2015.